Mechanical properties of FDM-printed PLA, PETG and their various sandwich structures, composites and recycled material structures

PhD Thesis

Rawabe Fatima Faidallah
PhD Student

Supervisor:
Dr. Oldal Istvan
Dr. Zoltan Szakal

Mechanical Engineering Doctoral School
MATE University – Gödöllő

2025

Doctoral school

Denomination: Doctoral School of Mechanical Engineering

Science: Mechanical Engineering Sciences

Leader: Prof. Dr. Gábor Kalácska, DSc
Institute of Technology
Hungarian University of Agriculture and Life Sciences,
Szent István Campus, Gödöllő, Hungary

Supervisors: Dr. Oldal Istvan, and Dr. Zoltan Szakal
Institute of Technology
Hungarian University of Agriculture and Life Sciences, Szent István Campus,
Gödöllő, Hungary

……..…… ….....……

Affirmation of supervisor Affirmation of head of school

CONTENTS

1. Introduction

The FDM process is worked by extruding thermoplastic material, which has heated up to its melting point through a nozzle, then depositing the extruded layers of materials on top of each other. Currently, FDM is considered the most widely used technology of all types of 3DP technology around the globe due to the low cost of the printer device. Platform temperature, nozzle size, layer thickness, printing direction, nozzle head temperature, printing speed, and raster angle are parameters that could be controlled to improve print quality. Other researchers looked at the details of many processing parameters. According to the research, a suitable bed temperature and regulated convective heat transfer conditions can increase the bonding strength of successive layers, improving the mechanical properties of printed objects. Many process parameters can be controlled when producing 3D-printed part structures. Since then, the influence of process parameter settings on the mechanical qualities (e.g., tensile, flexural impact, compressive, and fatigue strength) has been described in thorough for various production scenarios. These parameters were exhaustively investigated for different categories of materials.

This research will lead to better control and optimization of the 3D-printed polymer specimens using Fused Deposition Modeling (FDM) to investigate the impact of various tensile geometry shapes and printing parameters on the tensile properties. Additionally, Finite Element Method (FEM) simulations will be conducted to compare the different geometries.

The study also outlines the development of fiber-reinforced polymer composites. Laboratory re-manufacturing of pure filaments and filaments reinforced with fiber will be conducted to evaluate their tensile strength after recycling. furthermore, various compositions of functionally graded multi-materials with different gradient arrangements, including single and multiple gradients, will be created and examined for their tensile and compressive properties.

Moreover, rhombus and honeycomb structures will be designed and produced using FDM printing technology. The mechanical performance of these materials will be evaluated through tensile, three-point bending, and compression tests, with the failure modes of the specimens analyzed for each test. Furthermore, auxetic honeycomb cores will be examined to evaluate the effects of varying face layer thicknesses on three-point bending strength, considering both in-plane and out-of-plane core orientations. Compressive strength will be tested in both flatwise and edgewise positions. Additionally, finite element analysis (FEA) will be performed to gain deeper insights into stress distribution under bending and compressive loads.

This research aims to enhance the control and optimization of 3D printing parameters for polymers, while deepening our understanding of reinforcement polymer, sandwich structures, and multi-material compositions of polymeric elements. As an innovative cross-disciplinary study, it will gather unique testing data that integrates mechanical and chemical characteristics. Based on these results, recommendations will be developed for mechanical applications. The findings will be

precious for industrial producers increasingly utilizing advanced additive manufacturing technologies not only for rapid prototyping but also for the production of multi-material composite products.

2. Materials and methods

2.1. Design of experiment

In this research, FDM 3D printing technology was utilized to produce samples using thermoplastics in filament form. Two types of materials, neat (pure) polymers and composite polymers, were examined. Each material was employed to fabricate specimens with varying print parameters for different tests. These specimens underwent extensive mechanical testing and simulation, focusing on tensile, compressive, bending, and sandwich structure characteristics. The procedure and sequence of experiments conducted in this study are presented in the flowchart in Fig. 2.1. The following sections detail the procedures for material preparation, 3D printing of specimens, multi-material printing, and the various tests conducted for each material and method.

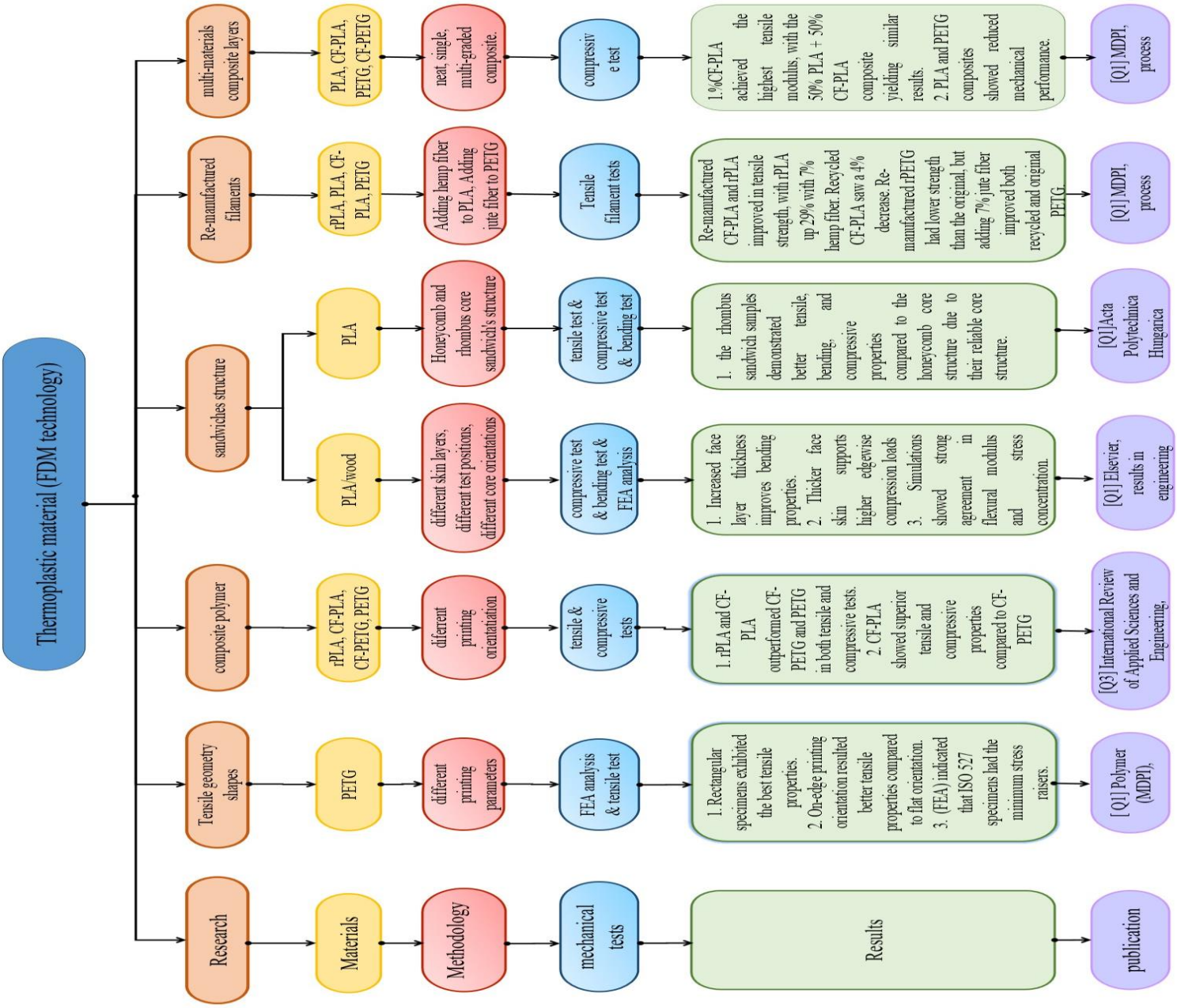

Fig. 2.1. Flowchart for the steps of the experiments

2.2. Manufacturing of 3D-printed specimens

As mentioned in section 2.1., two types of polymer materials were examined, neat and composite, for each 3D printing method. The following sections describe the details of producing the 3D-printed specimens for each material and technique used.

2.2.1 Different tensile geometry shapes

The specimens were manufactured using polyethylene terephthalate glycol (PETG) filament, The filament is black and has a diameter of 1.75 mm. The printing temperature and build platform temperature during the process were maintained at 230 °C and 70 °C, respectively. The

print speed, fill percentage, and number of perimeters were set as 60 mm/s, 100%, and 2 outlines, consecutively. In this research, the focus was on investigating the impact of build orientation as the primary manufacturing process parameter, while other parameters were kept constant to isolate its influence on mechanical performance. Table 2.1 contains the standards utilized for manufacturing the targeted specimens, along with the dimensions and other specifications of each specimen's type.

Table 2.1. Standard and specifications of each specimen type manufactured.

Standard	Width of narrow section [mm]	Width overall [mm]	Length overall [mm]	Thickness of narrow section [mm]	Thickness overall [mm]	Radius of curvature [mm]	Tab bevel angle [°]
ASTM D638	13	19	165	3	3	R76	-
ISO 527-2	10	20	150	3	3	R60	-
ASTM 3039/3039M	20	20	165	3	3	-	0°
ASTM 3039 angle	20	20	175	2	5	-	15°
ASTM 3039 angle	20	20	175	2	5	-	90°

All these tensile standard-shapes specimens created were printed in two build orientations (flat and on edge) to determine the effect of print orientation on the mechanical properties as well.

The experiments in this study aimed to investigate the influence of tensile test specimens' geometry on the mechanical characteristics and mode of failure. The Zwick/RoellZ100, a universal testing device, was employed to evaluate the tensile strength of the specimens. The tests were repeated three times to account for any potential variations. The obtained results were then averaged to obtain representative values. An extensometer, with very high precision (±1 μm within a 20–200 μm range), was used to capture even the smallest elongations, allowing for an accurate calculation of Young's modulus. During testing, each specimen was carefully secured in the grips and stretched at a steady speed of 3 mm/min along its length until it ultimately failed.

2.2.2 3D-printed carbon fiber-reinforced polymer composites and pure polymers

The experimental materials encompassed CFPLA, CFPETG, PETG, and recycled PLA (rPLA) filaments with a diameter of 1.75 mm. These filaments were reinforced with 10 wt.% carbon fibers, each having a fiber length of 100 μm. Table 2.2 presents the specific printing parameters for each material.

Table 2.2 Printing parameters employed for each material

Printing parameters	Material			
	PETG	CFPETG	rPLA	CFPLA
Layer thickness	0.2 mm	0.2 mm	0.2 mm	0.2 mm
Initial layer height	0.24 mm	0.24 mm	0.24 mm	0.24 mm
Print speed	60 mm/s	60 mm/s	60 mm/s	60 mm/s
Infill density	100%	100%	100%	100%
Platform temperature	70 ℃	75℃	60 ℃	45 ℃

Printing temperature	230 ℃	240 ℃	210 ℃	200 ℃
Nozzle diameter	0.4 mm	0.4 mm	0.4 mm	0.4 mm

Tensile test specimens, conforming to the ASTM D3039 rectangular shape (165 mm × 20 mm × 3 mm), were 3D-printed. For each material, samples were produced in two orientations: flat and on-edge. A total of 24 tensile test samples were printed (three from each orientation, utilizing identical print settings). Compressive test samples, adhering to ASTM D695, were created with a diameter of 13 mm and a length of 20 mm. The total count of compressive test samples reached 12. The design of these specimens was executed using SolidWorks software. A single specimen, selected from the three tested samples, was scrutinized to study the fracture interface in detail.

Tensile tests were carried out according to the ASTM D3039 standard, while compressive tests adhered to ASTM D695, utilizing a Zwick/Roell Z100 test machine. The tests were conducted at a 5 mm/min displacement rate, and the grip-to-grip distance was maintained at 99.8 mm. The force-displacement data were collected via computer using data acquisition software. Tensile properties assessed included tensile strength, tensile Young's modulus, and failure modes under prescribed conditions.

Compressive strength was computed by dividing the compressive load by the specimen's cross-sectional area. Compressive strain was determined using equation (3.4), and compressive modulus was calculated using equation (3.5).

$$\varepsilon = \frac{\Delta l}{l0}, \tag{2.1}$$

where Δl is the elongation and L_0 is the length of the sample.

$$E = \frac{\sigma}{\varepsilon}. \tag{2.2}$$

2.2.3 Re-manufactured filaments

- Material Specifications

` Recycled polylactic acid (rPLA) and polyethylene terephthalate glycol-modified (PETG) filaments, along with carbon fiber-reinforced PETG (CF-PETG) and carbon fiber-reinforced PLA (CF-PLA), were utilized for filament tensile testing.

This study also incorporated re-manufactured filaments of PLA, rPLA, and PETG. To enhance the mechanical properties of the re-manufactured PLA and rPLA filaments, hemp fiber was used as reinforcement. Similarly, jute fiber was employed for the re-manufactured PETG filaments. Comprehensive tensile property testing was subsequently conducted on these filaments.

Figure 2.2. presents a schematic roadmap that clarifies the distinction between the materials used, specifying which were purchased, which were employed in multi-material designs, and which were recycled, along with the tests performed on each group.

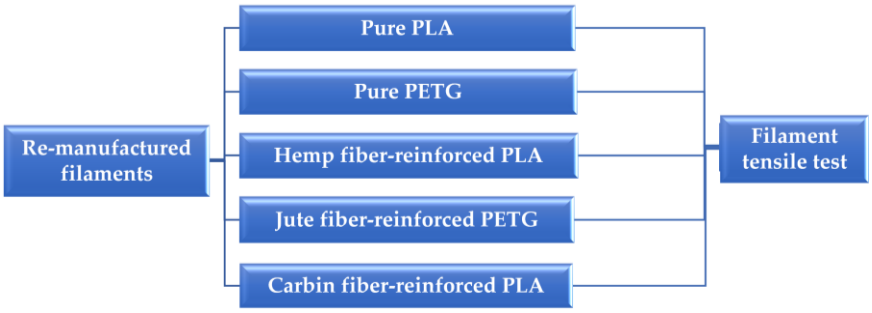

Fig.2.2. Schematic roadmap illustrating the categorization of materials used in the study: re-manufactured materials.

- Filament fabrication

The objective was to create new filaments by re-manufacturing the original commercially-produced filaments to evaluate their ultimate tensile strength (UTS) and compare these results with those of the initial filaments. The preparation process began with chopping the original filament into small particles utilizing a filament cutting machine. These particles were then fed into a single-screw extruder to produce new filaments.

In the Materials Science laboratory, a filament-cutting machine was utilized. A segment of the commercially-produced filament was sliced into pieces and placed into the machine's chamber. After securing the chamber to the apparatus, it was operated for seven seconds to generate the final particles. The cutting process generally produced particles in the 3–5 mm range, Fiber content was calculated using weight percent (wt.%), based on the formula:

$$Fiber\ wt.\% = \left(\frac{Weight\ of\ Fiber}{Weight\ of\ Fiber + Weight\ of\ PLA}\right) \times 100$$

This approach ensured that natural fiber reinforcement remained consistent at 7 wt.% across the samples.

Five materials PLA, rPLA, CF-PLA, PETG, and CF-PETG, were cut separately and prepared for manufacturing new filaments. The filament was created using a filament maker machine after being ground with the WŻ-1 grinder machine. PLA and PETG particles were fed into the machine's barrel and heated to specific temperatures. The extrusion temperatures were set to 185 °C and 200 °C for PLA and PETG polymers, respectively. The extrusion speed was set to the maximum level on the machine to ensure material melting. Inside the barrel, the rotating screw advanced the molten material, simultaneously mixing and blending it to maintain uniform quality. After the material was fully melted and homogenized, it was extruded through a die to produce filaments with a specified diameter of 1.75 mm. The filament was then cooled with a fan and readied for subsequent testing.

The filament diameter varied for each material. Table 2.3 shows the different diameters of the materials after they were re-manufactured and reinforced with natural fibers. The reduced filament diameter observed was likely due to challenges in controlling the fan speed and the rapid transition from the molten to solid state during extrusion. Additionally, the speed of the extruder played a role in this deviation, impacting the cooling rate and resulting in thinner filaments than expected.

Table 2.3. Diameters of the materials after re-manufacturing and reinforcing with natural fibers.

Specimens	Re-manufactured filament Diameters [mm]						
	PLA	rPLA	PETG	CF-PLA	PLA +Hemp	rPLA +hemp	PETG +Jute
1	1.1	1.2	1.4	1.2	1	1.3	1.3
2	1.2	1.2	1.5	1.2	0.9	1.3	1.3
3	1.2	1.2	1.5	1.2	0.7	1.2	1.3
4	1.1	1.1	1.5	1.1	0.7	0.9	1.2
5	1.1	1.1	1.4	1.2	0.9	1.2	1.2

The tensile properties of both original and re-manufactured filaments were evaluated at a crosshead speed of 5 mm/min, with at least five repetitions per case. Filaments of 300 mm length were tested using Bollard-style grips on a Zwick Roell Z100 machine, with a 150 mm gauge length between the grips. One grip was fixed while the other, connected to the load cell, applied displacement and recorded the force response.

2.2.4 Sandwich structures

2.2.4.1 PLA with honeycomb/rhombus core structures

PLA was chosen as the preferred material because of its growing popularity in FDM printing and its sustainable environmental characteristics. The filament used was 1.75 mm in diameter and black. As stated by the manufacturer, the filament's claimed qualities are tensile Young's modulus, ultimate tensile strength, strain at yield, and impact strength of 3.120 GPa, 70MPa, 5%, and 3.4 KJ/m^2, respectively, when tested according to ISO 527. The test samples were printed with an infill density of 100% and a layer thickness of 200 μm at a print speed of 60 mm/s. The printing and building plate temperatures were set as 210 °C and 60 °C, respectively. In the current study, the material utilized for both outer surfaces and inner structure was the same (PLA). Two sandwich structures, a honeycomb and a rhombus (see Figure 3.12) have been used. These structures were designed by the standards ASTM C393 and MIL-STD-401B. The designed specimens, with the honeycomb and rhombus sandwich structures, were prepared for the tensile, bending, and compression testing, as shown in Figure 2.3a, b, and c, consecutively. Magnification for the sandwich structures' core shape is demonstrated in Figure 2.3: honeycomb core (left) and rhombus core(right).

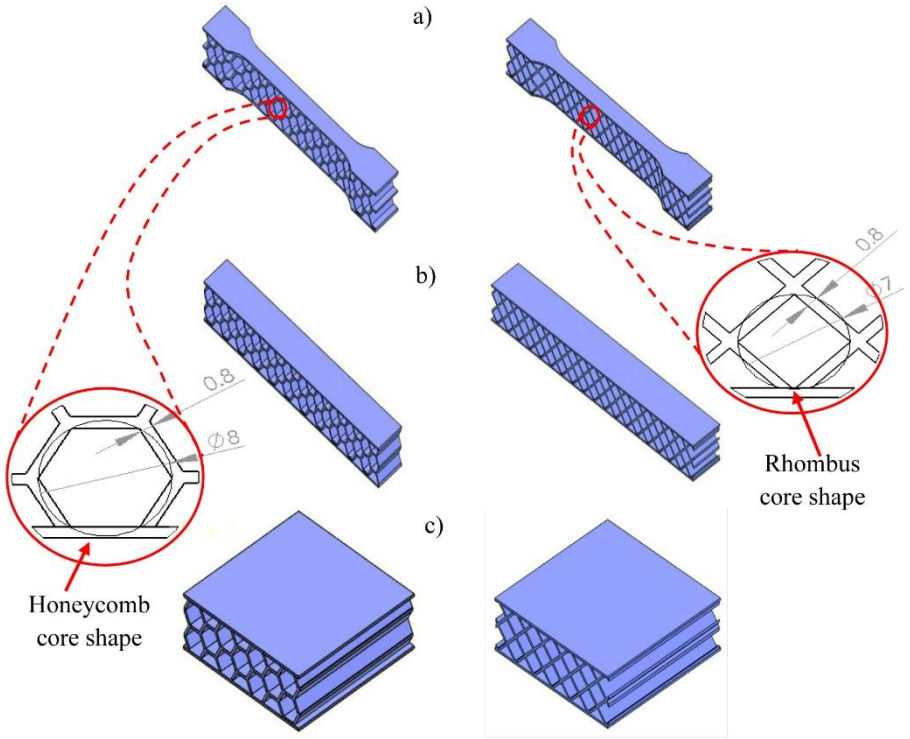

Fig.2.3. 3D models of the sandwich structure specimens of the honeycomb (left) and rhombus (right) patterns for a) tensile test, b) three-point bending test, and c) compression test

According to the appointed standards, the tensile and three-point bending tests specimens have the dimensions of 150 mm, 20 mm, and 15 mm for length, width, and height, respectively, with 0.75 mm as the thickness of the skin. Also, the compression test samples were designed with a length of 50 mm, a width of 50 mm, and a height of 15 mm, at a skin thickness of 0.75 mm. The specimens were built at an on-edge orientation. The chosen cell sizes were 8mm and 7 mm for the honeycomb and rhombus, respectively. In addition, the cell wall size for the honeycomb and rhombus was 0.8 mm (see core shape aside in Figure 2.3).

Table 2.4. Average values of mass and density (with its standard deviation (SD)) of specimens tested.

Structure	Mass (g)	$Volume_{solid}$ (mm^3)	$Density_{samples}$ (g/mm^3)	SD(±)(g/mm^3)
Tensile honeycomb	10.408	31500	$0.33*10^{-3}$	$6.73*10^{-6}$
Tensile rhombus	11.639	31500	$0.369*10^{-3}$	$4.93*10^{-7}$
Bend. Honeycomb	14.955	45000	$0.332*10^{-3}$	$1.47*10^{-6}$
Bend. Rhombus	17.228	45000	$0.382*10^{-3}$	$2.56*10^{-6}$
Com. Honeycomb	12.063	37500	$0.321*10^{-3}$	$1.22*10^{-6}$
Com. Rhombus	14.533	37500	$0.387*10^{-3}$	$1.15*10^{-6}$

Three repeated tests have been accomplished on the samples that were constructed for each configuration of the sandwich structure's core (honeycomb and rhombus). The following sections clarify the conditions and details of the tests performed.

- **Tensile testing**

The ISO standard 527 for tensile testing of polymers was used to assess the tensile properties of the built structures. The specimens were stretched at a steady speed of 1 mm/min along their main axis until they broke.

Equation (2.3) was used to calculate the tensile strength (σ_t) of sandwich specimens

$$\sigma_t = P_t/A_t, \tag{2.3}$$

where P_t stands for the ultimate load (N), while the sandwich specimen's cross-sectional area is represented by A_t (mm^2) in our study we chose the broken cross-section area where it was in the middle of the specimens. The cross-section area was calculated using SolidWorks software and was: 30 mm^2, and 32mm^2 for the honeycomb and rhombus, respectively
Tensile modulus (E_t) was calculated by Hooke's law

$$E_t = \sigma_t/\varepsilon, \tag{2.4}$$

- **Bending Testing**

The bending tests (three-points) were carried out following ASTM C 393 The crosshead speed of the tests was 1 mm/min until the specimen broke. In the three-point bending, the radius of supports and punch was 15 mm, and the span length was 100 mm. Equations (3.9-11) were used to calculate the values of bending strength (σ_b) as well as the bending modulus (E_b) of sandwich samples (Zaharia et al., 2020).

$$M = \frac{P_{max}*L}{4} \tag{2.5}$$

$$\sigma_b = \frac{M.y}{I}\ ,\ y = \frac{h}{2} \tag{2.6}$$

$$E_{bend} = \frac{L^3.F_{max}}{4.w.d^3.\Delta L} \tag{2.7}$$

Where: I: the moment of inertia (mm^4) calculated using solidwork software, M: Maximum Bending Moment (N.mm), P_{max}: the maximum applied load (N) (maximum applied load at the loading point of the beam, used to calculate the maximum bending moment and bending stress), *h:* the total thickness of the structure (mm), *L:* Length of the specimen between the supports (span length) (m), *d:* Thickness of the specimen (m), F_{max}: Maximum load applied (N) (is the force corresponding to the measured displacement used to calculate the bending modulus), ΔL: Deflection at the center (m), w is the specimen width (mm).

For the honeycomb and rhombus cores, homogenization was applied by considering them as effective solids with average density values, as reported in Table 2.4. This ensured consistency between the design geometry, the measured mass, and the effective cross-sectional properties used in the calculations.

- **Compression testing**

The sandwich structure specimens were compressed on a mechanical test machine. The tests were performed at a 1 mm/min crosshead speed. For reliable results, each lightweight sandwich construction investigated (honeycomb and rhombus) was subjected to three tests. The average cross-sectional area (A_{av}) was determined based on the relationship between mass, density, and geometry. This method enables accurate estimation of the effective load-bearing area, taking into account the internal core geometry and material usage.

For a solid PLA reference specimen of the same nominal dimensions (thickness t and length), the cross-sectional area is given by:

$$A_{PLA} = \frac{M_{PLA}}{\rho_{PLA} * t} \tag{2.9}$$

where: (A_{PLA}) cross-sectional area of a solid PLA specimen (mm^2), (M_{PLA})measured mass of the solid PLA specimen (g), (ρ_{PLA})density of solid PLA (g/mm^3), (t) specimen thickness (mm).

Similarly, the average cross-sectional area of a sandwich structure specimen (A_{av}) can be expressed as:

$$A_{av} = \frac{M_{str}}{\rho_{PLA}.t} \tag{2.10}$$

where M*str* is the measured mass of the printed sandwich specimen.

However, rather than directly measuring M*str* , it is often more convenient to relate it to the solid reference specimen using the density ratio:

$$\frac{\rho_{av}}{\rho_{PLA}} = \frac{M_{str}/_{V}}{M_{PLA}/_{V}} = \frac{M_{str}}{M_{PLA}} \tag{2.11}$$

Rearranging:

$$M_{str} = M_{PLA} * \frac{\rho_{av}}{\rho_{PLA}} \tag{2.12}$$

Substituting into the expression for A_{av}:

$$A_{av} = \frac{M_{PLA}}{\rho_{PLA}.t} * \frac{\rho_{av}}{\rho_{PLA}} \tag{2.13}$$

Since: $\frac{M_{PLA}}{\rho_{PLA}.t} = A_{PLA}$

The Final Simplified Formula:

$$A_{av} = A_{PLA} * \frac{\rho_{av}}{\rho_{PLA}} \tag{2.14}$$

The density (ρ_{av}) of the sandwich structure compression specimens is $0.32\times10^{-3}(g/mm^3)$ for honeycomb and 0.39×10^{-3} (g/mm^3) for rhombus, as listed in Table 2.4

Additionally, the density of the PLA material (ρ_{pla}), in the case of a solid bulk, is1.252×10^{-3} (g/mm^3).

To verify these analytical estimates, the specimen geometries were also modeled in SolidWorks, and the theoretical cross-sectional properties were extracted directly from the CAD models. This dual approach (analytical and CAD-based) ensured consistency between the design intent and the printed geometry.

2.2.4.2 Wood/PLA composites with re-entrant honeycomb core

The printing material used for both the face and core of the sandwich structure specimen e wood/PLA filament branded Spectrum with a diameter of 1.75 mm. The process was carried out at a temperature of 45 °C and 210 °C for the platform and printing head, respectively. The specimens were manufactured at a print speed of 60 mm/s, with a layer thickness of 0.2 mm, an infill density of 100%, and a line printing pattern, using a nozzle diameter of 0.4 mm.

The compression and 3-point bending test samples were manufactured according to ASTM C365-00, “standard test method for flatwise compressive properties of sandwich cores,” and ASTM C393, “standard test method for flexural properties of sandwich constructions.” Figure 2.4 is a magnification of the suggested and tested cell.

According to the specified standards, the bending test specimen had dimensions of 140 mm in length, 20 mm in width, and 10 mm in height. In addition, the compression test specimen was designed and manufactured with a length of 50 mm, a width of 50 mm, and a height of 10 mm. Bending and compression specimens were printed with different face layer (wall) thicknesses (0 mm, 0.8 mm, and 1.6 mm) in compression test specimens and (0.8 mm, 1.6 mm) in bending test specimens. The tensile specimen had dimensions of 150 mm in length, 20 mm in width, and 3 mm in thickness, with a gauge section length of 60 mm. For each test, the specimen was printed and tested three times, and the results in the paper are the average of three repeated test results. Table 2.5 lists the average densities for the specimens analyzed.

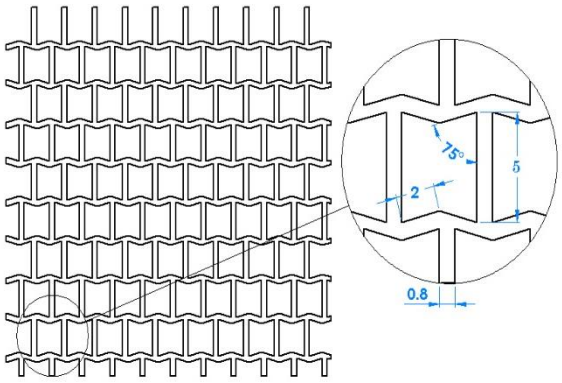

Fig.2.4. Design of re-entrant core unit cell.

Table 2.5. Average mass and density (with standard deviation) of the tested specimens.

Structure	Mass (g)	Volume $_{solid}$ (mm^3)	Density$_{struture}$ (kg/m^3)	SD (±) (g/mm^3)
Comp. – without face	8.584	7183.78	$1.2*10^{-6}$	$1.1*10^{-5}$
Comp. – with a face layer of 0.8 mm	12.51	11183.78	$1.12*10^{-6}$	$7.5*10^{-6}$
Comp. – with a face layer of 1.6 mm	16.82	15183.78	$1.1*10^{-6}$	$6.7*10^{-6}$
Bend. – with face layer of 0.8 mm, in-plane	12.94	11312.86	$1.14*10^{-6}$	$0.6*10^{-5}$
Bend. – with face layer of 1.6 mm, in-plane	17.33	15559.57	$1.113*10^{-6}$	$6.02*10^{-6}$
Bend. – with face layer of 0.8 mm, out-of-plane	13.11	10482.35	$1.25*10^{-6}$	$6.8*10^{-5}$
Bend. – with face layer of 1.6 mm, out-of-plane	17.35	14722.84	$1.18*10^{-6}$	$6.6*10^{-6}$

The average bending strength and bending modulus were determined by testing three specimens in each case with a 3 mm/min crosshead speed. Tests were carried out until the samples'

fracture points. The load was applied by a 7.5 mm diameter cylindrical central roller, with two exterior 5 mm diameter cylindrical rollers as supports, and the span length was 80 mm. Force–displacement measurements were recorded as the output of the testing machine. The three-point bending strength was tested with different thicknesses of top and bottom layers (0.8 and 1.6 mm) and different directions of the core structure (both in-plane and out-of-plane).

The compressive strength (both parallel (edgewise) and vertical (flatwise) to the surface) for different thicknesses of the top and bottom layers (0.8 and 1.6 mm) was examined on three specimens according to the ASTM C364/C364M standard. According to the standard, the crosshead speed for the compression test was set to 5 mm/min.

The simulations employed a linear elastic material model with the material defined as wood/PLA composite (as tested), with constants including a modulus of elasticity of 2085 MPa, a Poisson's ratio of 0.33, and a density of 1150 kg/m^3. The material chosen for the fixed supporting rollers and the loading central roller in the three-point bending analysis was stainless steel 316L. Loading was performed by applying a gradual displacement consistent with the strain rate of the experimental study to the upper cylinder (roller), while the two other cylinders (rollers) served as fixed supports. A single surface and friction contact (COF = 0.1) was established between core elements to prevent interpenetration during bending, and all contacts were assumed to be friction. A fixed support boundary condition was set at one end of the CAD-modeled samples to simulate the compression test, and a gradual displacement consistent with the experimental study's strain rate (5 mm/min and 3mm/min) was set at the other end. Model calibration used tensile-test data to set the elastic modulus of the printed material; validation relied on comparing bending/compression responses (load–deflection curves and peak load) between simulation and experiment.

2.2.5. Neat, single, and multi-gradient composites

In this investigation, four distinct types of polymeric filaments tailored for additive manufacturing were extruded. These categories included pure PLA and PETG polymers, as well as PLA and PETG polymeric composite filaments reinforced with 10 wt% carbon fiber. According to the material provider, the average length of the carbon fibers was 100 µm. The samples were created using a Bambu s1 MEX-type 3D printer, which is capable of additive manufacturing with up to four different materials in a layer-by-layer manner. In our experimentation, all four feedstock materials were used, with each material corresponding to a dedicated feeding system. The STL files of the samples were sliced into standard G-code for printing.

Tensile specimens of neat, single-gradient composites, and multi-gradient composites were manufactured. Table 2.6 provides details on the previous specimens and their corresponding notations.

Table 2.6 shows a List of Acronyms:

MEX - Material Extrusion	Material Extrusion
P	100% PLA
G	100% PETG
PCFP	50% PLA + 50% CF-PLA
GCFG	50% PETG + 50 % CF-PETG
PCFPP	25% PLA + 50% CF-PLA + 25% PLA
PCFGG	25% PETG + 50% CF-PETG + 25% PETG
CFP	100% CF-PLA

CFG	100% CF-PETG
PG	50% PLA+ 50 % PETG
GPG	25 % PETG + 50% PLA+ 25% PETG

The selection of the multi-material design samples was based on optimizing material properties for specific structural applications. The choice was influenced by prior studies that demonstrated the benefits of combining materials with different mechanical characteristics to enhance overall performance (Palaniyappan et al., 2023; Yermurat et al., 2023). The material properties of PLA and PETG produced under the specified printing parameters are outlined in Table 2.7.

Table 2.7 Printing settings employed while manufacturing the materials using Bambu 3D printer.

Printing settings	**PLA**	**PETG**	**CF-PLA**	**CF-PETG**
Layer height [mm]	0.12	0.12	0.12	0.12
Initial layer height [mm]	0.2	0.2	0.2	0.2
Wall loops	2	2	2	2
Top/bottom layers	2	2	2	2
Infill density [%]	100	100	100	100
Infill pattern	Rectilinear	Rectilinear	Rectilinear	Rectilinear
Printing temperature [°C]	210	220	220	240
Platform temperature [°C]	45	70	45	70
Printing speed [mm/s]	50	50	50	50

Tensile specimens of the various multi-material configurations, including those with gradient additives, were fabricated according to ISO 527-2-1B standards. These specimens were designed with dimensions of 150 mm in length, 20 mm in width, and 4 mm in thickness, and applied a tensile loading rate of 1 mm/min. Each set of 3D-printed samples underwent three repetitions of testing.

3.Results and Discussion

The experiments' results are presented in this chapter, as well as discussions suggesting the new findings. These include mechanical characteristics for different 3D printing FDM and materials (neat and composite for each technique) by assessing the results of sandwich structures, multi-materials, and testing (such as tensile, compressive, bending, and microstructure.

3.1 Different tensile geometry shapes

Various variables, as discussed in the literature, can effectively increase stiffness and strength. The major variables that influence deformations and deflections include material properties, layer binding, and FDM 3D printing parameters (mainly, infill pattern and build orientation).

The theoretical masses of the printed specimens were derived from the slicing software, whereas the actual masses were determined using a precision scale with an accuracy of ±0.01 g. In addition, the cross-sectional areas of the specimens were calculated to enable a more comprehensive comparison. The results, summarized in Table 3-1, reveal that the experimentally measured masses are consistently lower than their theoretical counterparts. This deviation, though minor, reflects the inherent variability of the printing process and highlights the subtle gap between digital design and physical realization.

Table 3-1 Comparison between theoretical masses, measured masses, and cross-section area.

Specimens	Flat		On-edge		Cross-section area (mm^2)
	real mass (g)	slicer- mass (g)	real mass (g)	slicer- mass (g)	
ASTM-D638	8.49	9.13	8.63	9.28	39
ASTM-D3039-0°	11.04	11.88	11.24	12.09	60
ASTM-D3039-15°	11.83	12.72	11.76	12.65	40
ASTM-D3039-90°	8.17	8.79	8.83	9.49	40
ISO 527	4.89	5.26	5.19	5.58	30

The load-displacement curves that were obtained from the tensile test for all examined shape geometry and orientations are shown in Figure 3.1. It is clear that the building orientation of the 3D printing parameter and the shape geometry has a significant impact on the values of force versus elongation. The results were divided into two diagrams according to the building orientations and the shapes of tensile standards examined. The highest applied loads required to reach the fracture, for the different shape geometry, were reported to the ASTM D3039-0° (for both flat and on edge), as shown in Figure 4.1.

In addition, the Young's modulus of ASTM D3039-0° was 26.74% and 40.15% higher than the ISO 527 geometry shape (the lowest modulus) for the flat and on-edge orientations, respectively. In comparison between ASTM D638 and ISO 527, the average of ASTM D638 specimens was 14% and 21% higher than the ISO 527 geometry shape for flat and on-edge orientations, consecutively.

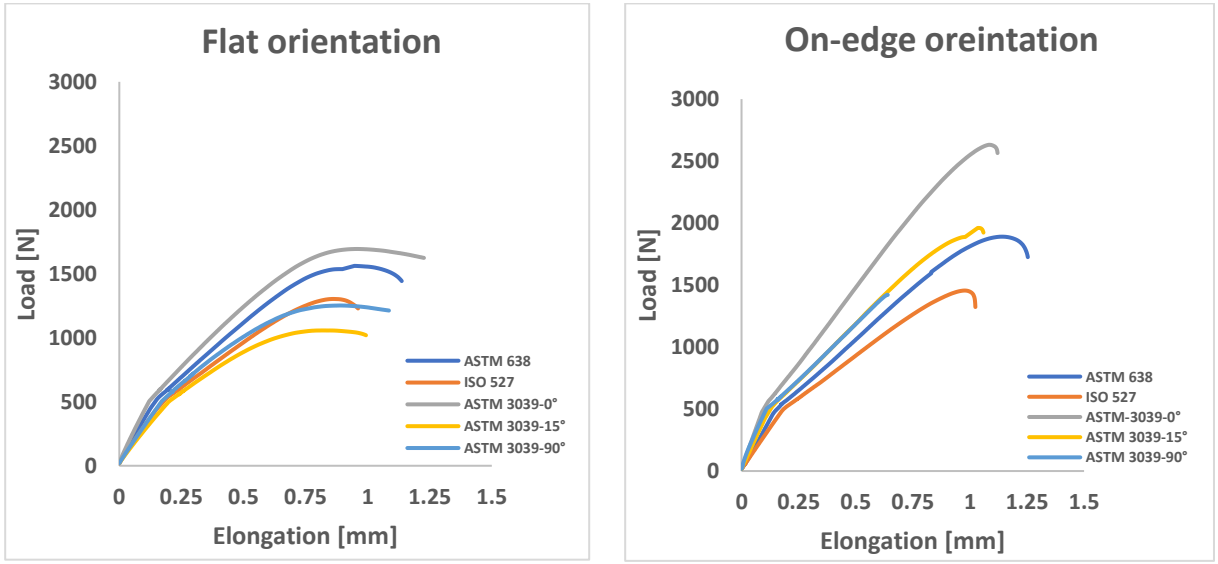

(**a**) (**b**)

Fig.3.1. Load-displacement curves for (a) flat building orientation and (b) on-edge orientation.

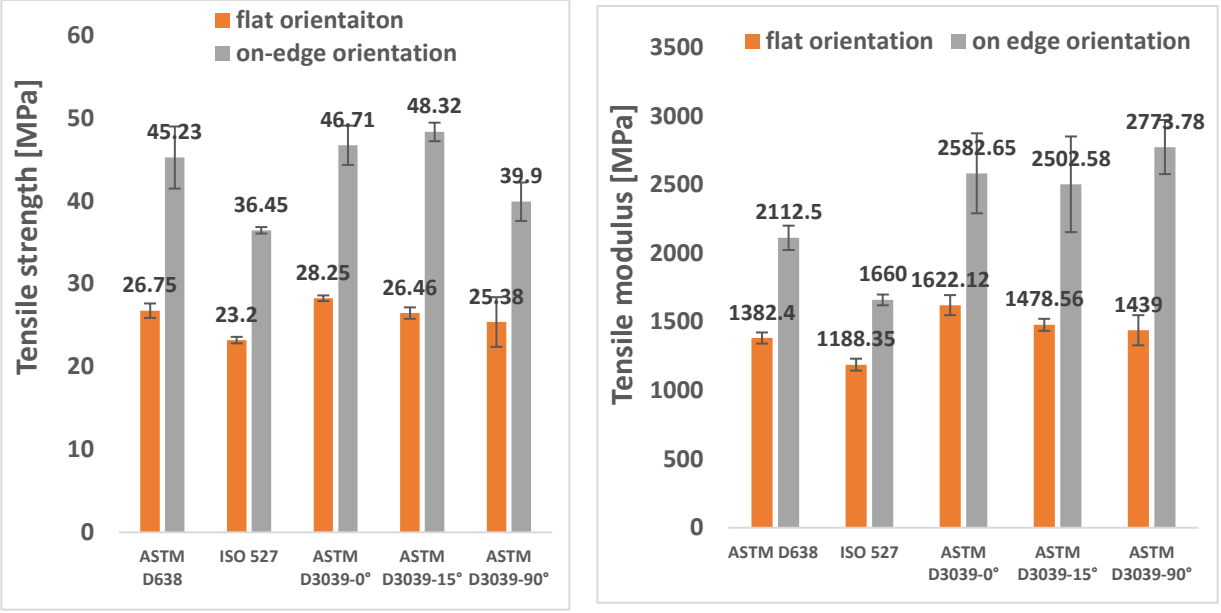

(a) **(b)**

Fig 3.2. Results of different geometry shape specimens during tensile test for flat and on-edge build orientations (a) tensile strength, (b) tensile Modulus

To distinguish in which geometry shape and printing parameter the specimen's failure was better, the broken area was given a percentage out of 100% (called the good breakage area) considering the fracture place from the middle of the sample; the closer to the middle the higher the percentage, and vice versa. Therefore, if the broken area is near the neck/edge, then it is not considered to get the good fracture. Figure 4.4 shows the percentage of the good breakage area based on the specimens' fractures.

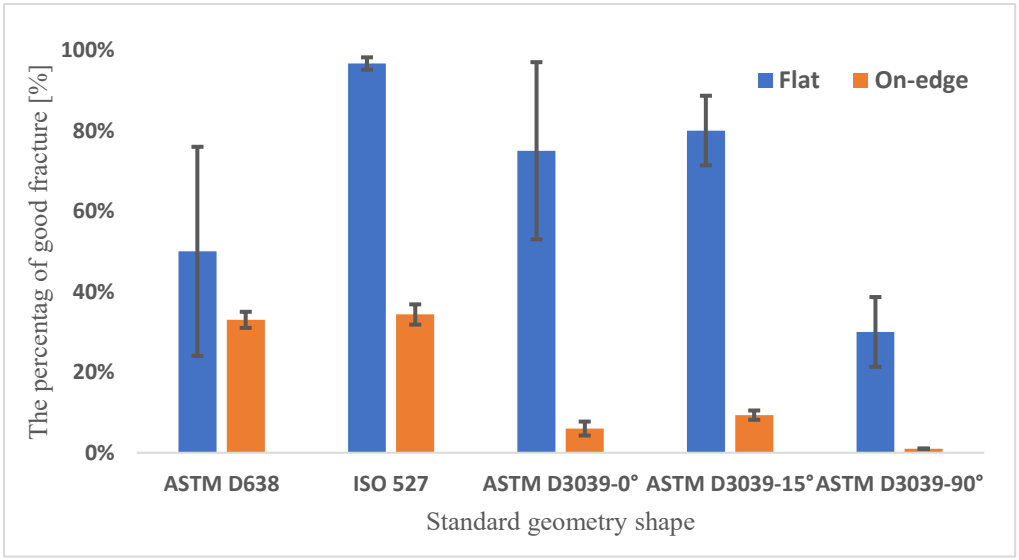

Fig.3.3. The percentage of good breakage area of specimens.

3.1.2. Numerical results

The specimens were manufactured in the on-edge orientation, where print layers align vertically with the principal loading direction. This orientation was selected as it has been shown to enhance tensile strength and stiffness compared to upright (Z-axis) builds, due to better filament alignment and interlayer bonding.

To ensure the validity of mechanical properties testing, the geometry of the testing specimen must not influence its actual mechanical properties. The presence of any stress risers can introduce artificial stress concentrations, leading to inaccurate experimental results. In structural analysis, the stress-strain behavior of a material can be represented using either linear or nonlinear curves. In linear analysis, the material's stress-strain curve is assumed to be linear, while nonlinear analysis involves implementing a digital representation of the true material stress-strain curve. In this research, linear and nonlinear modeling methods were employed to evaluate the ability of linear models to accurately capture physical phenomena. A Young's modulus of 5250 MPa was considered for the linear models. The nonlinear models incorporated additional material properties such as a yield strength of 70 MPa and a tangent modulus of 10 MPa. Table 3.2 presents the maximum Von Mises stress for each specimen and the shape-specific stress-increasing effects using a stress value of 70 MPa in the boundary conditions.

Table 3.2. Von Mises stress values of different tensile geometry specimens.

Specimen	Linear Model		Nonlinear Model	
	Maximum Stess (MPa)	**Multiplier factor %**	**Maximum Stess (MPa)**	**Multiplier factor %**
ASTM D638	115.64	39.47	89.17	21.50
ASTM D3039-0°	149.11	53.05	77.18	9.30
ASTM D3039-15°	77.27	9.41	71.51	2.11
ASTM D3039-90°	337.1	79.23	71.33	1.86
ISO 527-2	77.18	9.30	71.32	1.85

The results presented in Table 3.2 provide valuable insights into the behavior of the tested specimens. It is evident that the linear stress-strain model tends to overestimate the equivalent stress, while the nonlinear model yields values that are closer to the stress values used in the simulation settings. This discrepancy highlights the importance of using an accurate representation of the material's stress-strain curve for reliable simulations.

3.2 3D-Printed carbon Fiber-reinforced polymer composites and pure polymers

The investigation aimed to enhance stiffness and strength through various parameters, as highlighted in the literature. Tensile and compressive property graphs were constructed by averaging the values from three replicate samples for each condition.

3.2.1 Tensile properties

Figure 3.4 portrays the tensile force-elongation curves for the four materials across distinct building orientations. Notably, the 3D printing building orientation and the material composition distinctly influenced the force-elongation profiles. The results were segregated into two curves based on the building orientation, each delineating the material's behavior concerning the

orientation. Discrepancies among the materials may be attributed to distinct material properties and the interlayer adhesion generated during FDM-based specimen construction.

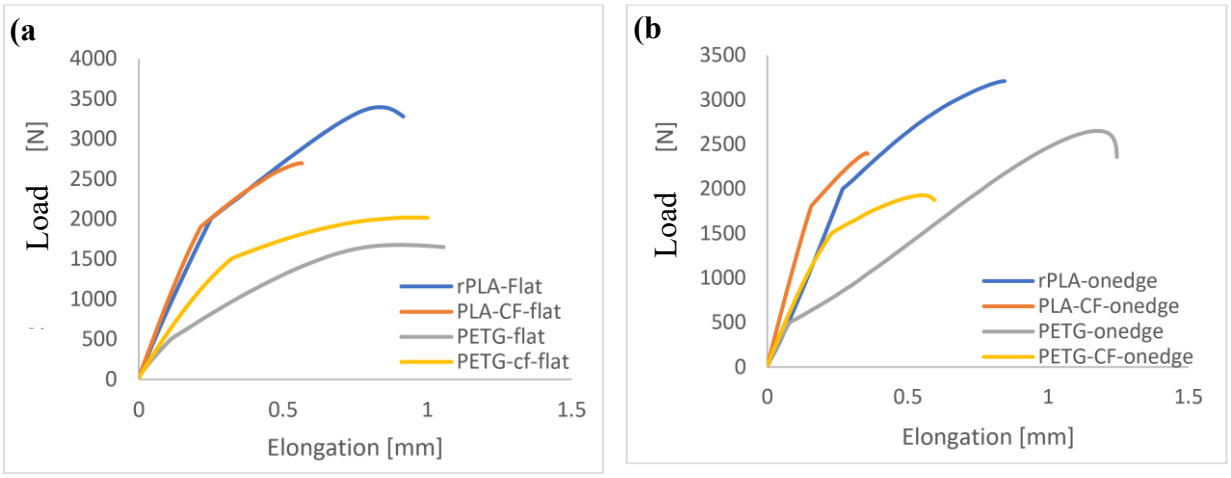

Fig. 3.4 Load-elongation curves for: (a) flat build orientation, (b) on-edge orientation

The rPLA exhibited a maximum force load of 3393 N and 3202 N for flat and on-edge orientations, respectively, surpassing the carbon fiber reinforced PLA. Moreover, PETG and CFPETG exhibited differential responses based on orientation. In the flat orientation, CFPETG demonstrated superior force load due to aligned fibers, displaying 20% higher force than PETG. Conversely, in the on-edge orientation, CFPETG recorded 37% lower force than PETG.

Figure 3.5 summarizes the average tensile test results. In terms of tensile strength, rPLA outperformed other materials with both building orientations. Specifically, rPLA exceeded CFPLA, PETG, and CFPETG by 30%, 100%, and 65.7% for flat orientation, and by 39.2%, 21%, and 77.6% for on-edge orientation, respectively. For tensile modulus, CFPLA displayed superior values for both orientations, indicating lower elasticity in rPLA compared to CFPLA. The comparison between CFPLA and CFPETG revealed CFPLA's tensile strength to be 26.6% and 27.6% higher for flat and on-edge orientations, respectively. Concerning tensile modulus, CFPLA exceeded CFPETG twofold for flat orientation and threefold for on-edge orientation, aligning with the results reported by (Rangisetty & Peel, 2017).

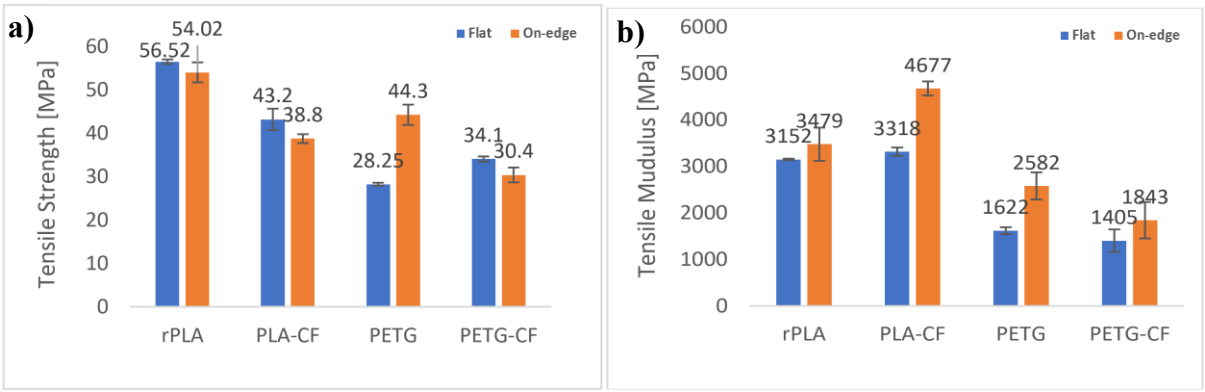

Fig. 3.5 Tensile test results (a) tensile strength, (b) Tensile Modulus.

Several studies have reported that short-fiber reinforcements in FDM parts often reduce ductility and may even lower tensile strength compared to neat polymers. This is commonly attributed to poor fiber–matrix adhesion, increased porosity, and fibers acting as stress concentrators when not aligned with the loading direction. Such factors help explain why rPLA outperformed CFPLA and CFPETG in tensile strength, particularly in the on-edge orientation where fiber alignment with the tensile axis is less favorable. In these cases, fibers may act more as inert fillers than true reinforcements, especially when discontinuous and randomly distributed. The reduction in elongation at break is consistent with the increased brittleness reported in literature when fibers hinder polymer chain mobility.

For PETG, natural specimens showed a pronounced orientation effect, with higher tensile strength in the on-edge orientation due to better filament alignment and reduced reliance on interlayer bonding. In contrast, short-fiber reinforcement minimized these orientation-dependent differences by enhancing stress transfer and interlayer adhesion, thereby reducing the anisotropy typically observed in FDM-printed materials.

3.2.2 Compressive properties

Figure 3.6 illustrates the compressive force-elongation curves for the four materials across three specimens. Notably, rPLA and CFPLA displayed the highest and near-highest force. Conversely, CFPETG samples exhibited the lowest compressive force among the materials. Table 3.3 provides average compressive results for all tested materials. Figure 3.7 showcases average maximum compressive stress, Young's modulus, and maximum compressive strain. rPLA demonstrated a maximum compressive stress of 82.3 MPa, surpassing CFPLA by 23.7%. PETG's compressive strength (53.7 MPa) aligned with reported literature values, ranging from 41 to 98 MPa (Amza et al., 2021). PETG and CFPETG exhibited lower compressive deformation, while rPLA demonstrated the largest maximum deformation, in accordance with (Hsueh et al., 2021). The latter found that PLA's mechanical properties surpassed those of PETG, except for thermal deformation.

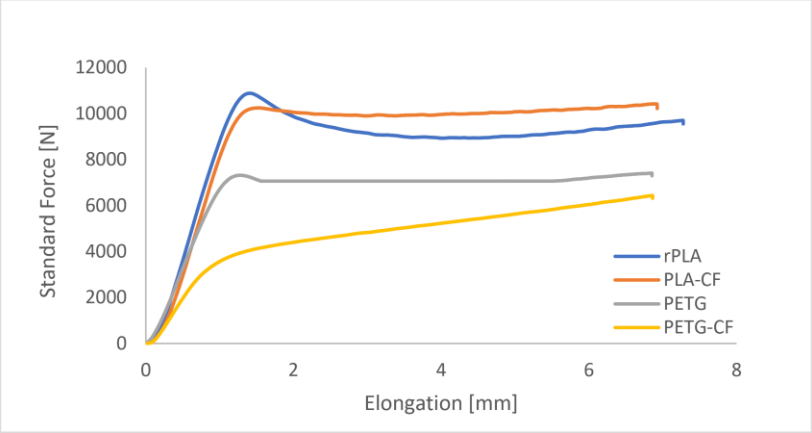

Fig. 3.6 Force-elongation curves for compressive tests

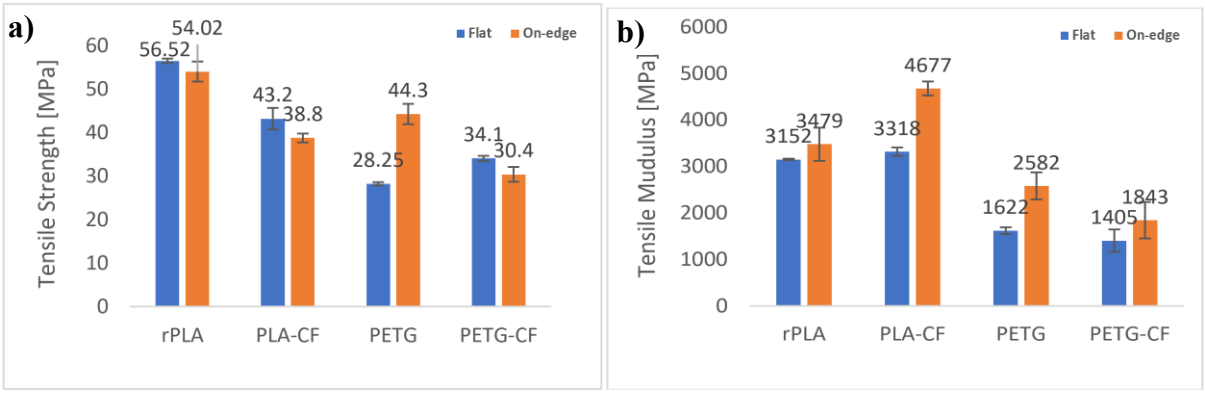

Fig. 3.7 Tensile test results (a) tensile strength, (b) Modulus strength

Table 3.3 The compressive properties for the materials examined

Compressive Properties	rPLA	CFPLA	PETG	CFPETG
Compressive strength (MPa)	82.3	66.5	53.7	49.3
Compressive modulus (MPa)	358.1	290.4	241.8	221.8
Compressive strain (%)	2.30	2.29	2.23	2.22

3.3 Re-manufactured filaments

3.3.1 Original filament tensile test

Tensile testing was conducted on the original filament material, which had not undergone extrusion during the printing process. Figure 3.8 presents the stress-strain curves for the five different filament materials. The figure provides one representative result out of the three tests conducted for each material.

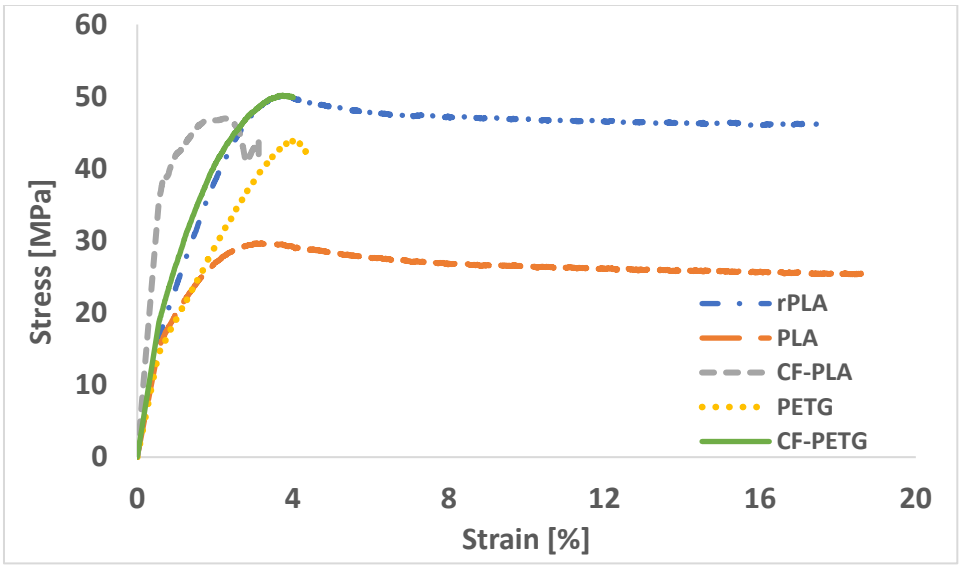

Fig 3.8. Stress-strain curves for the original (non-printed) materials.

The CF-PETG filament exhibited a maximum stress of 50.14 MPa, closely matching the stress of rPLA filaments. The stress of CF-PETG was higher than that of rPLA, PLA, CF-PLA, and PETG by 0.2%, 70%, 6.7%, and 14.4%, respectively. The CF-PETG filament demonstrated consistent stress resistance throughout the specified strain range. In contrast, the other filaments experienced a reduction in stress resistance after reaching their respective peak stress levels. Compared to the tensile strength values provided by the manufacturer, the tensile strength of PLA, rPLA, PETG, and CF-PLA decreased by 30%, 20%, 28%, and 27%, respectively. This reduction can be attributed to several factors, including variations in environmental conditions (such as humidity and temperature), differences in testing equipment or setup (e.g., grip type, alignment, or loading speed), and the storage conditions of the filament prior to testing (see Table 2.3 for manufacturer data).

3.3.2 Re-manufactured filament tensile test

Additionally, jute fiber-reinforced PETG underwent re-manufacturing and testing in this segment. Notably, the re-manufactured PLA and rPLA exhibited superior tensile strength compared to the original filaments, which can be attributed to the consistent layer bonding in the PLA samples. However, the recycled CF-PLA showed a 4% reduction in strength compared to the original filaments. This decrease in tensile strength is likely due to the formation of fiber clusters during recycling, weakening the adhesive bond between the PETG and carbon matrix. The clusters reduce the mechanical properties of the composite by impairing interlayer adhesion. Regarding PETG filament, the recycled PETG exhibited lower strength than the original filaments. On the contrary, incorporating 7 wt% hemp fiber into PLA and rPLA filaments and re-manufacturing them resulted in filaments with superior tensile strength compared to the original ones. In the case of white PLA with hemp filaments, the tensile strength surpassed that of the original filaments and pure recycled PLA by 29% and 26%, respectively. Furthermore, adding 7 wt% hemp fiber to rPLA increased its tensile strength by 7% compared to the original rPLA filament, though it resulted in a 6% decrease in tensile strength compared to re-rPLA. Moreover, adding 7 wt% jute fiber to PETG enhanced the tensile strength by 12% and 15% for the original and re-manufactured PETG

filaments, respectively. A comparison between the maximum applied load and ultimate tensile strength (UTS) for both the original and re-manufactured filaments is shown in Table 3.4.

Table 3.4 Maximum applied load and tensile strength, values for the original, re-manufactured, and reinforced filaments.

Filaments	**$F_{original\ filament}$** [N]	**$F_{re\text{-}filament}$** [N]	**$UTS_{re\text{-}filament}$** [MPa]	**$UTS_{original\ filament}$** [MPa]
re-PLA	71.51 ±2.7	18 ±1.2	30.6 ±1.8	29.7 ±3.2
re-rPLA	120 ±4.8	50 ±1.7	58.6 ±2.5	50 ±3.7
re-PETG	105 ±2.5	72 ±3.1	42.43 ±2.3	43.86 ±2.6
re-CFPLA	113 ±3.4	66.8 ±2.6	42.4 ±3.1	47 ±3.6
re-PLA+Hemp	-	18 ±1.1	38.5 ±0.9	-
re-rPLA+Hemp	-	50 ±2.8	53.5 ±2.7	-
re-PETG+Jute	-	62.38 ±3.2	49 ±3.3	-

3.4 Sandwich Structures

3.4.1 PLA with honeycomb/rhombus core structures

3.4.1.1 Tensile performance of sandwich structures

Figure 3.9a shows the load-displacement curves that were obtained from the tensile test of the honeycomb and rhombus sandwich structures. In terms of the tensile strength, which ranged between 19.49 and 23.01 MPa, the better values were from rhombus core sandwich structures (see Figure 3.9b). The increased tensile strength of these specimens is due to their reliable core structure, which had more contact sites at the fracture area under tensile stress than the honeycomb core construction (see Figure 3.9). Therefore, the applied load was distributed across a larger area, resulting in higher resistance to failure. In contrast, honeycomb sandwich structures had the best tensile Young's modulus of 599 MPa compared to rhombus (440 MPa), as shown in Figure 3.9c.

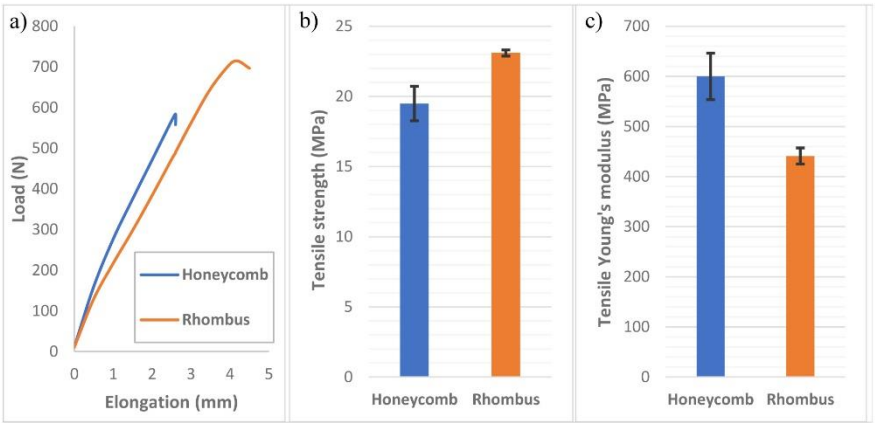

Figure 3.9 Tensile test result of sandwiches structure specimens, a) load-displacement curves, b) tensile strength values, and c) Young's modulus values

3.4.1.2 Three-Point bending performance of sandwich specimens

The flexural performance of the lightweight sandwich constructions (honeycomb and rhombus), including bending strength, and bending modulus, was investigated using this test approach. The load-displacement curves of test specimens for three-point bending have two main stages, as Using Equations (2.5-2.7) and the sandwich specimen dimensions, the test machine software

automatically determined the bending modulus and bending strength, which are the most essential three-point bending aspects.

Three-point bending results were better for the rhombus compartive with honeycomb core sandwich structure. The maximum force reported was about 381 N at a displacement of 4.47 mm of rhombus core specimens, according to the curves shown. In terms of the bending strength, Figure 3.10b exhibits that the rhombus core sandwich models had a bending strength average value of 40% higher than that of the honeycomb core sandwich samples. Furthermore, the bending Young's modulus of rhombus specimens was twice as high as that of honeycomb specimens (see Figure 3.10c).

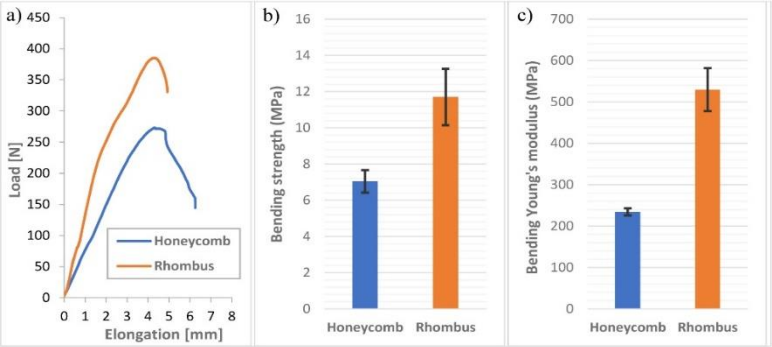

Figure 3.10 Three-point bending test results of sandwich structures, a) load-displacement curves, b) bending strength, c) Young's modulus of bending

3.4.1.3 Compression behaviour of sandwich structures

It is evident from Figure 3.11a that the load-displacement responses are generally linear until the core shear starts, at which point there is a dramatic reduction in load. The maximum force (roughly 5850 N) was found in the rhombus core structures (at an elongation of 1.6 mm) until unredeemable damage in this sandwich structure occurred. However, for the honeycomb structure, irreversible damage occurred when the load force reached 2820 N at 1.35 mm elongation.

The results of compressive stress and modulus are presented in Figure 3.11b and Figure 3.11c, respectively. Again, the rhombus core sandwich structure offered the best performance as the average of its compressive strength (70 MPa) was 35.4% higher than that of the honeycomb (45.8 MPa) and its compressive modulus (891.015 MPa) was 15.54 % better than the honeycomb (752.513 MPa). The dense network of its structures, which also caused these specimens to weigh more, is responsible for the outstanding performance of rhombus core specimens.

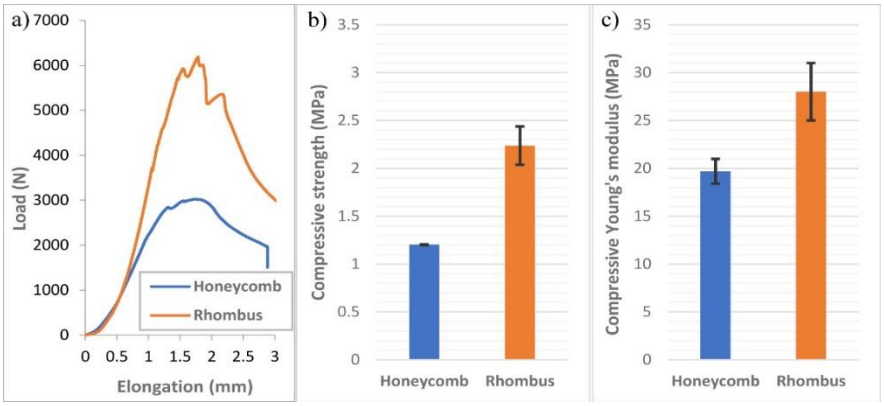

Fig 3.11 Compression test results, a) load-elongation curves, b) compressive strength, and c) Young's modulus of compression

3.4.2 Wood/PLA composites with re-entrant honeycomb core

The tensile strength of 3D-printed solid material is 29 MPa. Young's modulus was calculated at 2085 MPa from the stress-strain curve.

3.4.2.1 Experimental bending test

Experimental stress-strain curves obtained from the bending tests for all examined re-entrant core orientations (in-plane (vertical, V) and out-of-plane (horizontal, H)) are shown in Figure 4.26a. The samples with in-plane core position and 1.6 mm face layer exhibited the highest stress, reaching 124 MPa. This stress level surpassed that of the in-plane core position with a 0.8 mm face layer by 30% and exceeded the out-of-plane core positions with 1.6 mm and 0.8 mm face layers by 26% and 195%, respectively. Conversely, the lowest stress was observed in the out-of-plane core position with a 0.8 mm face layer.

Figure 3.12b shows the flexural modulus, the specimen with a 1.6 mm face layer thickness and in-plane core position (1.6 V) exhibits the highest E modulus at approximately 374.47 MPa. The out-of-plane core position (H) with a 0.8 mm face layer has an E modulus of about 265 MPa, which is the lowest among all tested configurations. It is important to note that the better performance of the in-plane core position is not only due to increased material presence under loading but also due to the unique structural benefits of the re-entrant design. This design optimizes material distribution, which enhances performance in the in-plane direction compared to typical porous structures.

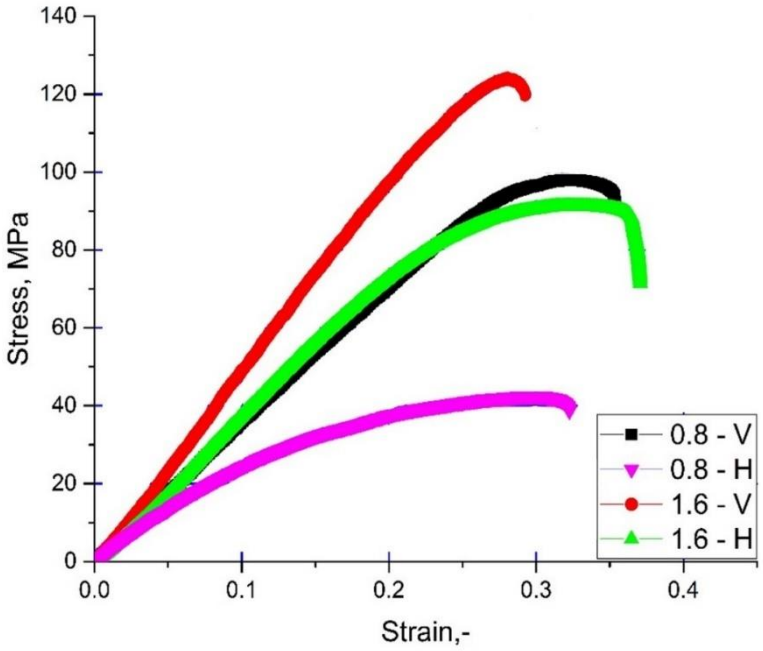

(a)

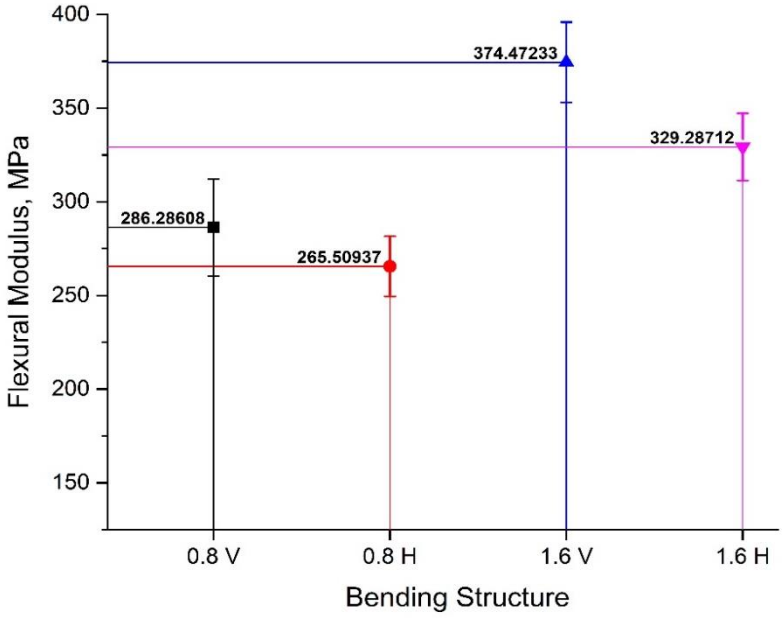

(b)

Fig 3.12. (a) Bending stress-strain curves and (b) flexural modulus of the bending re-entrant honeycomb structure

3.4.2.2 Experimental compressive Test

Since the areas subjected to compressive stress in the printed specimens are not fully filled with material, the actual cross-sectional areas were calculated using SolidWorks software, as calculated in Table 3.5. Here, A_S is the smallest subjected area and A_L is the largest subjected area.

Table 3.5. Cross-sectional areas corresponding to various compressive positions, as shown in Figure 4.29.

Compressive test position	A_S	A_L
Flatwise with (0, 0.8, 1.6 mm) face layer	(a) 718.38	
Edgewise with (0 mm) face layer, without face	(b) 80 mm^2	(c) 453.4 mm^2
Edgewise with (0.8 mm) face layer	(d) 168mm^2	(e) 473.7 mm^2
Edgewise with (1.6 mm) face layer	(f) 248 mm^2	(g) 641.6 mm^2

Figure 3.13 illustrates the stress-strain curves derived from two distinct positions in the compressive test. The outcomes reveal variations in the mechanical properties of the materials under stress between these two positions (edgewise and flatwise). In the edgewise position, the maximum stress is delineated across two cross-section areas: small (A_S) and large (A_L) cross-sections. Specifically, the edgewise configuration with a 1.6 mm face layer displayed a maximum stress of 44 MPa for V_S and 15 MPa for V_L. where V_s represents the compressive load applied over the small area, and V_L corresponds to the compressive load applied over the large area. Contrastingly, specimens lacking a face layer achieved a peak stress of 48 MPa in the flatwise test position (Figure 3.13a). This value surpasses the maximum stress obtained by specimens with 0.8 mm and 1.6 mm face layers by 20% and 23%, respectively. This is because removing the face layer can significantly enhance the structure's performance by increasing flexibility, reducing weight, and improving stress distribution within the core material. These factors collectively contribute to a higher maximum load capacity.

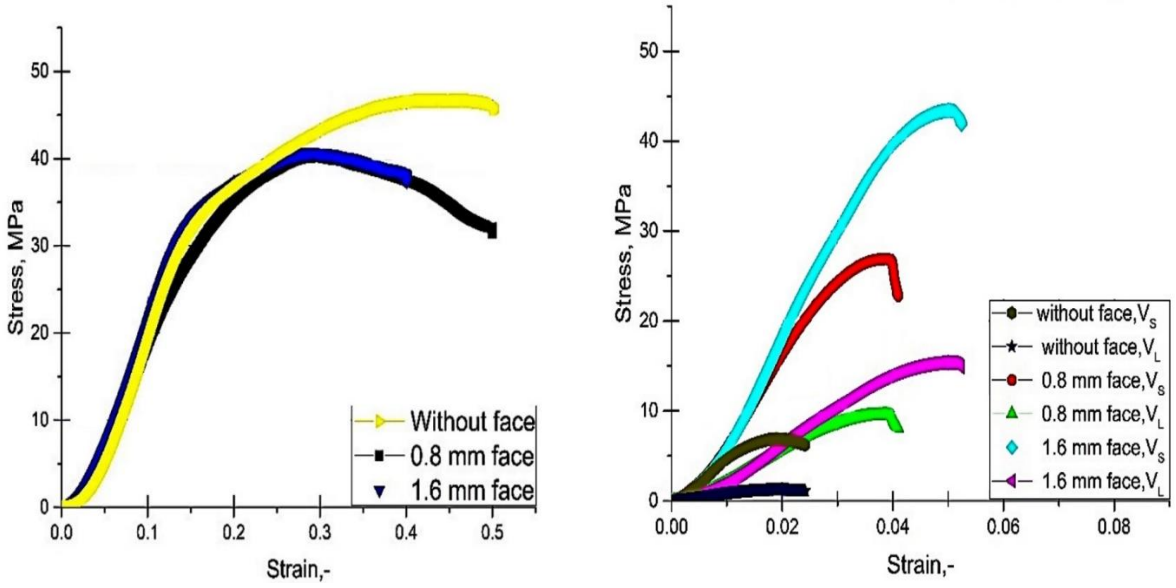

(a) (b)

Fig 3.13. Stress-strain curves of the compression specimens: (a) flatwise (vertical to the surface), (b) edgewise (parallel to the surface)

3.4.2.3 Numerical analysis of Bending and Compression Tests

By comparing simulations results with experimental data, we can validate and enhance our comprehension of material behavior under different loading conditions. Figure 4.33 represents the comparison of experimental flexural modulus and simulated flexural modulus. The outcomes of the simulation and the experiment are in good accord. Flexural experimental modules show lower values than flexural simulated modules, which may be due to the existence of layer air gaps, and impurities which make it difficult to achieve homogeneity of the mechanical properties (Rafsanjani et al., 2015).

Table 4.6 presents the maximum bending strength (MBS) and flexural modulus (E) of experimental and simulated works. Table 4 presents the maximum compressive strength (MCS) and the compressive modulus of elasticity (E) for all compressive-tested specimens, for both experimental and simulated results.

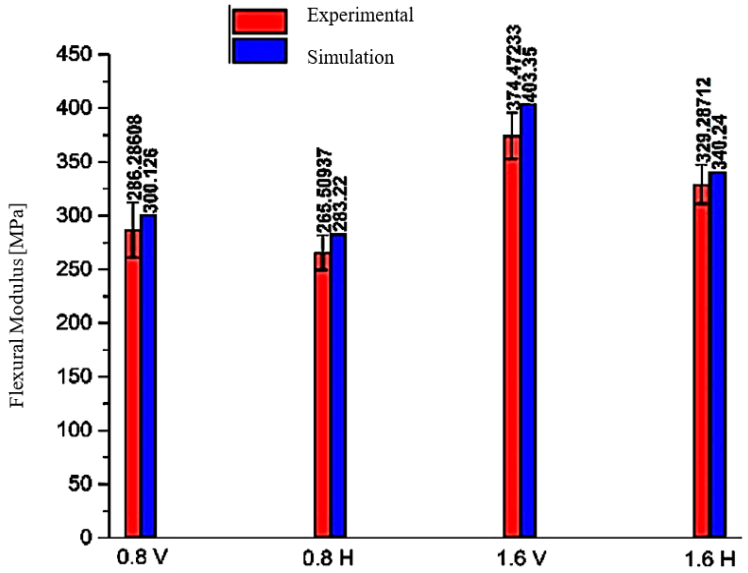

Fig 3.14. Comparison of experimental and simulated flexural modulus

Table 3.6. Maximum bending strength (MBS) and flexural modulus (E) values for different bending positions.

Specimens, Position	**MBS experimental (MPa)**	**E experimental (MPa)**	**E numerical (MPa)**
In-plane with 0.8 mm face layer	91.19	286.29	300.13
In-plane with 1.6 mm face layer	124.02	374.47	403.35
Out-of-plane with 0.8 mm face layer	42	265.51	283
Out-of-plane with 1.6 mm face layer	98.02	329.29	340.24

In the case of the compression test, discrepancies between the experimental modulus of elasticity and simulated modulus of elasticity were observed. The maximum deviations of the simulated modulus of elasticity compared to the experimented modulus of elasticity are around 17% and 10% in the cases of flatwise and edgewise, respectively. The Comparison of the

experimental compression modulus of elasticity and simulated modulus of elasticity in the compression tests is shown in Figure 3.15.

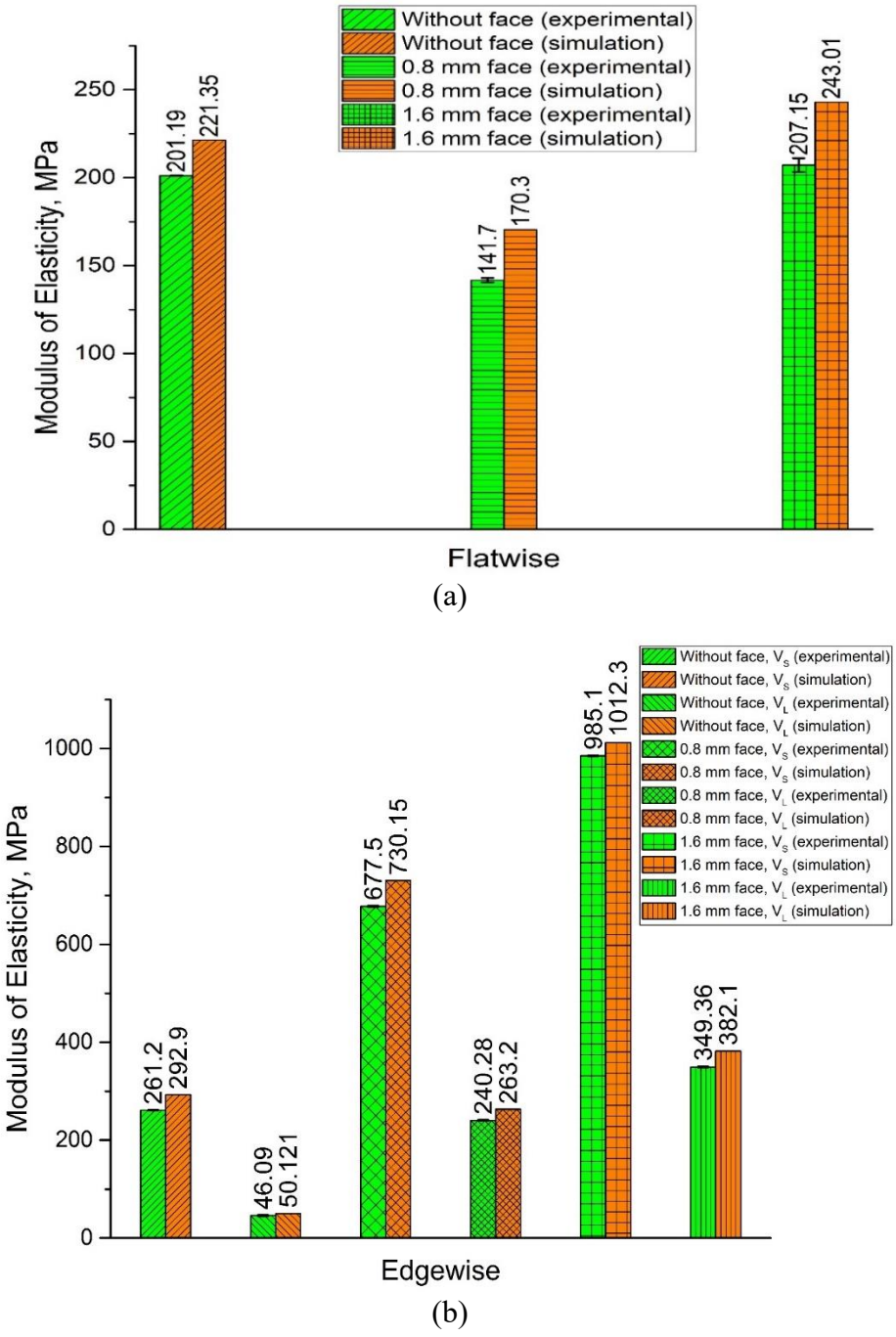

Fig 3.15. Comparison of experimental and simulated compression modulus of elasticity: (a) flatwise, (b) edgewise.

Table 3.7 Maximum compressive strength (MCS) and compressive modulus of elasticity (E) values at various compressive positions.

Specimens and position	$MCS_{experimental}$ (MPa)	$E_{experimental}$ (MPa)	$E_{numerical}$ (MPa)
Flatwise without face layer (0 mm)	46.7	201.2	221.35
Flatwise with (0.8 mm) face layer	40.2	141.7	170.3
Flatwise with (1.6 mm) face layer	40.7	207.15	243
Edgewise without face layer (0 mm), As	6.91	261.2	292.9
Edgewise without face layer (0 mm), A_l	1.22	46.1	50.12
Edgewise with face layer (0.8 mm), As	26.8	677.5	730.15
Edgewise without face layer (0.8 mm), A_l	9.5	240.28	263.2
Edgewise with face layer (1.6 mm), As	43.4	985.1	1012.13
Edgewise without face layer (1.6 mm), A_l	15.4	349.36	382.1

3.5. Neat, single, and multi-gradient composites

3.5.1 Tensile performance of neat, single, and multi-gradient composites

Figure 3.16 presents the tensile properties of neat, single and multi-graded materials. Specifically, Figure 3.16(a) shows the tensile force-elongation curves for the materials. Figures 3.16(b) and 3.16(c) display the Young's modulus (E modulus) and tensile strength of different graded composites for the PLA, CF-PLA, PETG, and CF-PETG materials. In addition, Table 3.8 provides a detailed comparison of the tensile properties of the examined specimen materials. The results indicate that the tensile strengths of the neat materials are quite similar, with neat PLA exhibiting a slightly higher tensile strength than PETG by 0.03%. Generally, PLA is recognized for its higher tensile strength compared to PETG, making it a more rigid material with lower elongation at break. Conversely, PETG demonstrates higher elongation at break, making it more flexible, impact-resistant, and less brittle than PLA. For specimens composed of 100% layers, the tensile strength of CF-PLA was 0.04% higher than that of neat PLA. In contrast, the tensile strength of CF-PLA decreased by 65% compared to neat PETG. This reduction could be attributed to the introduction of carbon fibers, which potentially increases the occurrence of microvoids within the printed layers, thereby diminishing the overall tensile strength of the composite.

To compare the tensile strength of various additively manufactured specimens, the highest tensile strength, 47.4 MPa, was achieved by specimens composed of PCFPP. This was close to the specimens manufactured by PCFP, which showed a tensile strength of 46.2 MPa. Specimens manufactured with multi-layers of CFPLA and PLA composite showed improved tensile strength, with increases of 4% for PCFP and 7% for PCFPP compared to neat PLA. Conversely, specimens manufactured with multi-material layers of PETG and CF-PETG experienced a reduction in tensile

strength compared to neat PETG. The tensile strength decreased by 4% for GCFGG and by 5% for GCFG. These results demonstrate the distinct impacts of material compositions on tensile strength, showcasing the advantages of CFPLA in enhancing tensile properties while also highlighting the challenges of integrating carbon fiber with PETG.

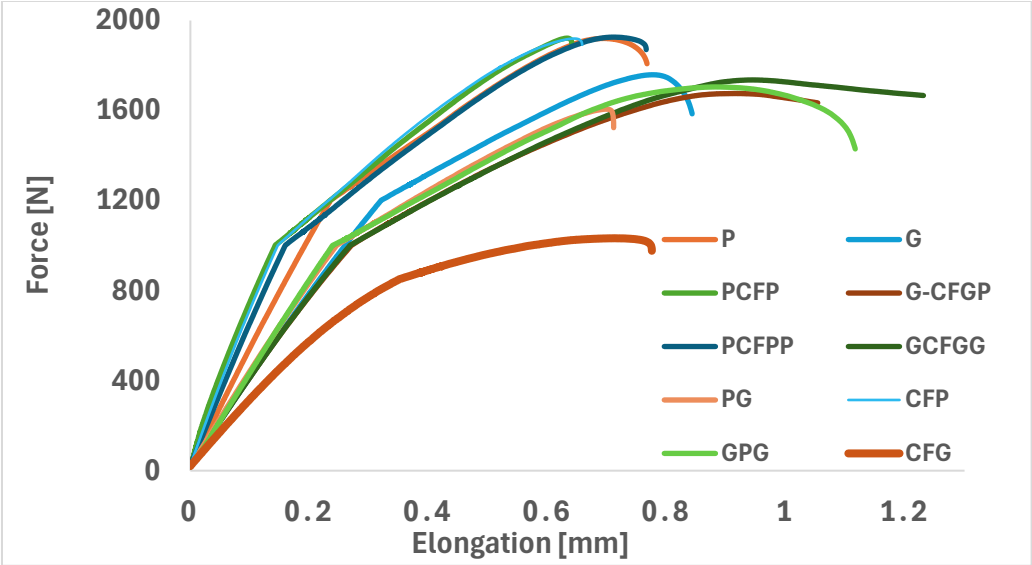

(a)

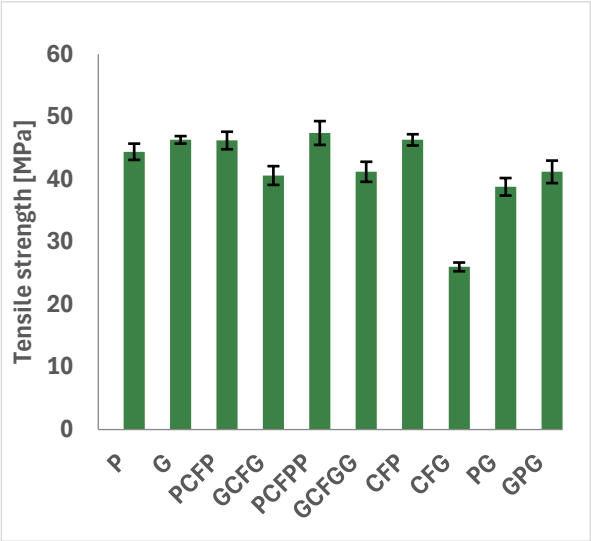

(b)

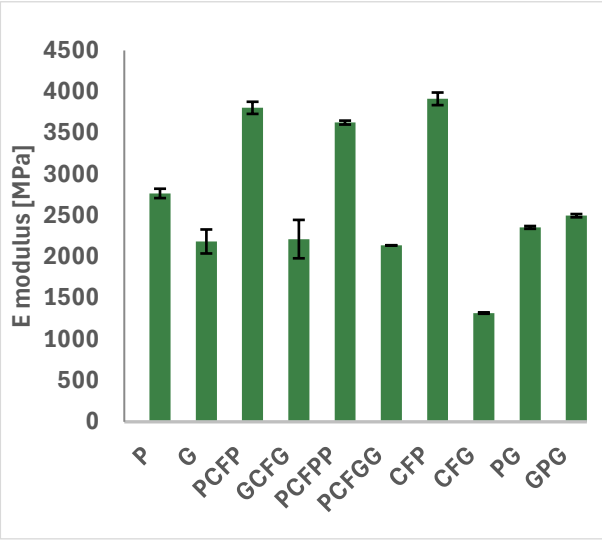

(c)

Fig 3.16. Tensile testing results: (a) Load-elongation curves, (b) tensile strength values, and (c) E-modulus measurements.

For the composite specimens of PLA and PETG, the highest tensile strength was observed in the GPG specimens, reaching 41.19 MPa. This value is lower than the tensile strength of specimens manufactured with 100% layers of neat PLA and neat PETG. The results suggest that while there are certain benefits to using a layered composite of PLA and PETG, the tensile strength of such composites does not always surpass that of using either material alone. This underscores

the importance of optimizing the adhesion and intermolecular forces between different materials in composites to fully leverage their individual advantages. Enhancing the interfacial adhesion between PLA and PETG may facilitate the development of composite materials that optimally exploit the complementary mechanical properties of each constituent, representing a promising direction for future research.

For the tensile modulus, specimens manufactured with 100% CF-PLA layers exhibited the highest tensile modulus at 3914 MPa. Among the single and multi-graded PLA + CFPLA multi-material composites, the specimens composed of 50% PLA + 50% CF-PLA showed a relatively high tensile modulus of 3805 MPa, outperforming other multi-layered composites. Conversely, the lowest tensile modulus was observed in the specimens manufactured with 100% CF-PETG, with a value of 1318 MPa. Furthermore, the multi-layered composites of PLA and PETG displayed reduced mechanical properties, which can be attributed to inadequate interfacial bonding between the two polymers. This poor adhesion likely stems from the differences in optimal printing temperatures and material characteristics of PLA and PETG, which hinder the formation of a strong, cohesive bond during the AM process.

Table 3.8. Mechanical qualities of the single, multi-graded, and neat materials.

Materials	Maximum applied load [N]	Elongation at maximum applied load [mm]	Maximum stress [MPa]	E-modulus [MPa]
P	1920 ±65.2	0.69 ±0.07	44.4 ±2.5	2768 ±96
G	1759 ±119.5	0.77 ±0.09	42.9 ±3.19	2185 ±105
PCFP	1921.7 ±82.1	0.63 ±0.13	46.2 ±3.56	3805 ±173
GCFG	1675 ±96.7	0.91 ±0.05	40.6 ±1.47	2214 ±151
PCFPP	1926.2 ±102.6	0.71 ±0.04	47.4 ±2.41	3626 ±127
GCFGG	1736 ±67.7	0.94 ±0.16	41.2 ±1.53	2138 ±208
CFP	1919.8 ±76.1	0.64 ±0.15	46.3 ±1.62	3914 ±76
CFG	1032 ±82.8	0.7 ±0.06	26 ±2.61	1318 ±84
PG	1606 ±99.7	0.69 ±0.09	38.8 ±2.2	2356 ±169
GPG	1705 ±52.9	0.88 ±0.17	41.19 ±1.84	2498 ±197

The multi-material composite designs explored in this research can be applied to other polymer-based materials, providing valuable insights for the additive manufacturing and materials science communities. These findings encourage further exploration into sustainable materials for real-world applications like short-life-cycle or non-critical components such as accessories, tool holders, robotic effectors, educational models, disposable items, and general-purpose prototyping, where PLA and PETG's properties, such as ease of printing and rigidity, can be effectively utilized.

4. New scientific results

The mechanical characteristics of 3D-printed polymers, polymer composites, sandwich structures were comprehensively investigated in this study. The following points are noteworthy to be mentioned:

1. ***Mechanical Characterization of 3D-Printed Polymers: Role of Re-Manufacturing and Fiber Reinforcement***

I investigated the mechanical behaviour of both original and re-manufactured polymer and fiber-reinforced filaments used in 3D printing. The study encompasses a range of materials, including PLA, recycled PLA (rPLA), PETG, carbon fiber-reinforced PLA and PETG (CF-PLA, CF-PETG), as well as natural fiber-reinforced variants. Among all tested materials, **recycled PLA (rPLA)** demonstrated the most favorable mechanical properties, outperforming both pure and carbon fiber-reinforced variants in tensile and compressive strength, by up to 100% and 67%, respectively.

Further analysis revealed that re-manufacturing impacted tensile performance depending on the material type. While recycled CF-PLA showed a slight 4% reduction in strength due to fiber clustering, re-manufacturing CF-PETG proved more challenging due to extrusion inconsistencies.

In a further effort to enhance sustainability, natural fibers were introduced as reinforcement agents. The inclusion of 7 wt% hemp fiber in rPLA resulted in a 7% increase in tensile strength relative to the original material. Likewise, the addition of 7 wt% jute fiber to PETG improved its tensile strength by 12% compared to the original and by 15% compared to its recycled form. Although variability in filament diameter posed challenges for compatibility with certain 3D printers, the production of mechanically reliable samples was successfully achieved and tested.

2. ***Influence of the core orientation and face skin thickness on bending and compressive properties.***

I offered valuable insights into the mechanical behavior of 3D-printed re-entrant honeycomb sandwich structures, focusing on the effects of face layer thickness, core orientation, and loading conditions. I confirmed that increasing the thickness of the face skin significantly enhances bending strength and stiffness.

Additionally, the in-plane core orientation demonstrated higher bending strength compared to the out-of-plane orientation. In flatwise compression, the re-entrant core without a face layer remarkably sustained a maximum load, this improved flexibility and stress distribution, enhancing compressive strength, suggesting that lighter structures can withstand substantial loads.

Moreover, I performed numerical simulations that closely matched the experimental data, with only minor deviations likely due to material heterogeneity. The simulations accurately identified stress concentration zones, which aligned with failure areas observed under microscopy, further supporting the results.

3. ***Effects of neat, single, and multi-graded composites on tensile strength properties***

In this research, I investigated the tensile properties of various neat and composite materials, specifically neat PLA, PETG, CF-PLA, CF-PETG, and their combinations.

I demonstrated that multi-layer composites comprising CF-PLA and PLA exhibited an increase in tensile strength of 4% for the PCFP configuration and 7% for the PCFPP configuration compared to neat PLA. Additionally, I found that the tensile strength of multi-material PETG and CF-PETG composites declined relative to neat PETG, with reductions of 4% for the GCFGG configuration and 5% for the PCFP configuration.

I also observed that the highest tensile strength among the composite specimens made from PLA and PETG was found in the GP configuration, although this strength was lower than that of the neat materials.

Furthermore, my microscopic analysis revealed brittle fractures in the PLA specimens and clear separation between layers in the PLA/PETG composites, indicating poor adhesion at the interfaces.

5. Conclusion and Suggestion

In this study, the mechanical behavior of FDM printing pure PLA/PETG, and PLA/PETG composites were reviewed exhaustively. Based on the assessment of the results, the following observations can be drawn:

- The ASTM 3039 standard geometry demonstrated superior tensile properties compared to the dumbbell-shaped samples with curved edges, as defined by ISO 527 and ASTM 638.
- Numerical analysis of stress concentration: The ISO 527-2 specimens showed reduced stress concentration near the gripping area, with higher stress localized in the narrow gauge section, away from the clamping zones.
- The Young's modulus and UTS are maximum at On-edge print orientation due to its robust construction, while elongation at break is better at Flat orientation.
- The choice of standard should be application-specific: ISO 527 is preferable for fracture behavior studies, while ASTM D3039 is better suited for assessing tensile performance
- Carbon fiber-reinforced PLA (CF-PLA) obtained better compressive and tensile properties than carbon fiber-reinforced PETG polymer.
- rPLA filament obtained better compressive and tensile properties in compared with CF-PLA, CF-PETG, and PETG polymer (CF-PETG).
- Among the original filaments, CF-PETG exhibited the highest filaments tensile strength, surpassing PLA, PETG, CF-PLA, and rPLA.
- In the case of re-manufactured filaments, the results were more varied. Recycled PLA (rPLA) demonstrated a significant 29% increase in tensile strength when reinforced with hemp fibers, outperforming its original filaments. Conversely, recycled CF-PLA showed a slight 4% decrease in tensile strength compared to its original filaments. For PETG, the re-manufactured filaments exhibited lower tensile strength than the original; however, the addition of jute fibers significantly enhanced the performance of both recycled and original PETG.
- The rhombus sandwich samples demonstrated better tensile, compressive, and flexure strength compared to the honeycomb structure, attributed to their robust core design
- Increasing the face layer thickness significantly enhanced the bending properties of both in-plane and out-of-plane re-entrant sandwich structure core specimens.
- Thicker face skin enhances the maximum applied load when compressed from the edgewise, creating a more pronounced gap between the face skin and the core.
- Flatwise compressive tests indicated that the re-entrant structure, when lacking a face layer, exhibited the highest maximum load capacity.

- Tensile tests of multi-material layers revealed that % CF-PLA exhibited the highest modulus of elasticity, with the 50% PLA + 50% CF-PLA composite showing nearly equivalent results. In comparison, 100% CF-PETG displayed the lowest modulus, suggesting possible issues with fiber-matrix interaction.

Further innovation in core designs for sandwich structures is also needed, particularly through exploring advanced auxetic or lattice cores that could improve strength-to-weight ratios and resistance to impact. Another important direction is to evaluate the performance of FDM-printed materials under diverse environmental conditions such as changes in temperature, humidity, and chemical exposure. Long-term studies should also be conducted on the degradation of the mechanical properties of FDM composites under cyclic loading and environmental stresses. Moreover, exploring methods for recycling printed components and composites would reduce environmental impact and promote circular material use.

The findings of this study also highlight several avenues for advancing numerical modeling. Extending finite element modeling by adopting fully anisotropic constitutive laws, incorporating multi-orientation testing, and implementing cohesive-zone adhesion would provide a more comprehensive representation of both global structural responses and localized failure mechanisms in FDM parts. Comparative analyses with pure PLA specimens are recommended to isolate and evaluate the specific effects of recycling and reinforcement on material integrity and structural performance. In addition, developing optimized re-extrusion methods to produce dimensionally stable reinforced filaments would enable stronger correlations between filament properties and the mechanical behavior of printed structures.

Further investigation into sandwich structures should also incorporate cyclic and vibration-based flatwise compression tests to capture progressive damage and collapse mechanisms in cores with out-of-plane orientations. Linear regression should be applied across the elastic region of tensile curves in future studies to provide a more statistically robust estimation of Young's modulus, thereby strengthening the reliability of inter-specimen comparisons. Benchmark testing of solid specimens would also be beneficial in quantifying the trade-offs between strength and weight, while simultaneously highlighting the structural efficiency and lightweight advantages of rhombus and honeycomb cores for practical engineering applications.

Additionally, the implementation of cohesive zone models (CZM) to explicitly capture interlayer adhesion, particularly under loading conditions parallel to the build orientation such as edgewise compression, would refine predictive capacity for delamination and failure mechanisms, complementing the global behavior analyses performed in this work.

Finally, Improved interfacial compatibility between PLA and PETG may lead to composites with enhanced mechanical performance, highlighting an important focus for subsequent research efforts

6. Summary

This study provides a comprehensive evaluation of the mechanical behavior of Fused Deposition Modeling (FDM) 3D-printed components, with a particular focus on the influence of print orientation, geometric configurations, sandwiches structures and multi-material compositions. The

research investigates ASTM D3039 rectangular specimens printed at 0°, 15°, and 90° angles and compares them against other tensile samples in accordance with ASTM and ISO standards. All specimens were fabricated using polyethylene terephthalate glycol (PETG) material and were tested in two distinct print orientations: flat and on-edge. Finite Element Analysis (FEA) was employed to identify stress concentrations and weak points in each configuration. The study also extends to evaluating tensile and compressive behavior of various material compositions, including recycled polylactic acid (rPLA), PLA with carbon fiber reinforcement (CF-PLA), pristine PETG, and PETG reinforced with 10 wt.% carbon fiber (CF-PETG). Furthermore, the performance of pre-consumer recycled PETG and rPLA filaments reinforced with varying percentages of hemp and jute fibers was assessed. Additionally, the study examines the mechanical properties of sandwich structures using rhombus and honeycomb core geometries made from PLA. The research also analyzes the effect of face layer thickness variations (0 mm, 0.8 mm, and 1.6 mm) on re-entrant honeycomb core sandwich structures made from wood/PLA composite filaments. Material characterizations included bending tests, compressive tests, and finite element analysis (FEA) to identify stress concentration areas.. Finally, the mechanical behavior of multi-material composites, including neat PLA and PETG, single-graded combinations, and multi-gradient configurations, was thoroughly evaluated.

The ASTM D3039 specimens printed at 0° in the on-edge orientation exhibited the highest tensile properties, whereas the flat orientation showed superior results in terms of failure area. ISO 527-2 specimens consistently demonstrated lower tensile properties across all orientations. FEA analysis revealed minimal stress concentrations in ISO 527-2 specimens, with higher stress localized in the narrow regions, isolated from the gripping zones. Among the material compositions, rPLA exhibited the best overall tensile and compressive performance, outperforming both CF-PLA and CF-PETG, regardless of print orientation. PLA with carbon fiber reinforcement showed superior mechanical properties compared to its PETG counterparts. Recycled PLA filaments reinforced with hemp fibers significantly improved tensile strength compared to the original PLA, and jute-reinforced PETG showed notable strength improvements over the pristine PETG and its recycled versions. For the sandwich structures, rhombus cores displayed superior mechanical behavior, with enhanced tensile, bending, and compressive strengths compared to honeycomb configurations. Increasing face layer thickness greatly improved resistance to bending, and specimens with an in-plane orientation demonstrated higher bending strength than those with out-of-plane orientation due to increased material engagement. In flatwise compressive testing, specimens without a face layer exhibited the highest compressive strength due to greater displacement capacity. In contrast, edgewise compression tests indicated significant buckling behavior of the face sheet, with maximum stress increasing proportionally with face layer thickness. These results were validated through FEA, closely aligning with experimental findings. Lastly, multi-material composites generally showed lower mechanical performance compared to neat PLA and PETG due to reduced interlayer adhesion. These findings underscore the need for optimizing core architectures, material combinations, and reinforcement strategies to enhance the mechanical properties of 3D-printed composite structures for advanced manufacturing applications.

7. Reference

1. Amza, C. G., Zapciu, A., Constantin, G., Baciu, F., & Vasile, M. I. (2021). Enhancing Mechanical Properties of Polymer 3D Printed Parts. *Polymers*, *13*(4), 562. https://doi.org/10.3390/polym13040562

2. Hsueh, M.-H., Lai, C.-J., Wang, S.-H., Zeng, Y.-S., Hsieh, C.-H., Pan, C.-Y., & Huang, W.-C. (2021). Effect of printing parameters on the thermal and mechanical properties of 3d-printed pla and petg, using fused deposition modeling. *Polymers*, *13*(11), 1758.
3. Palaniyappan, S., Annamalai, G., Sivakumar, N. K., & Muthu, P. (2023). Development of functional gradient multi-material composites using Poly Lactic Acid and walnut shell reinforced Poly Lactic Acid filaments by fused filament fabrication technology. *Journal of Building Engineering*, *65*, 105746. https://doi.org/10.1016/j.jobe.2022.105746
4. Rafsanjani, A., Akbarzadeh, A., & Pasini, D. (2015). Snapping Mechanical Metamaterials under Tension. *Advanced Materials*, *27*(39), 5931–5935. https://doi.org/10.1002/adma.201502809
5. Rangisetty, S., & Peel, L. D. (2017). The Effect of Infill Patterns and Annealing on Mechanical Properties of Additively Manufactured Thermoplastic Composites. *Volume 1: Development and Characterization of Multifunctional Materials; Mechanics and Behavior of Active Materials; Bioinspired Smart Materials and Systems; Energy Harvesting; Emerging Technologies*, V001T08A017. https://doi.org/10.1115/SMASIS2017-4011
6. Yermurat, B., Seçgin, Ö., & Taşdemir, V. (2023). Multi-material additive manufacturing: Investigation of the combined use of ABS and PLA in the same structure. *Materials Testing*, *65*(7), 1119–1126. https://doi.org/10.1515/mt-2022-0368
7. Zaharia, S. M., Enescu, L. A., & Pop, M. A. (2020). Mechanical performances of lightweight sandwich structures produced by material extrusion-based additive manufacturing. *Polymers*, *12*(8), 1740.